

# 1 Have you ever seen the rain? Observing a record 2 convective rainfall with national and local monitoring 3 networks and opportunistic sensors

4 Louise Petersson Wårdh<sup>1,2\*</sup>, Hasan Hosseini<sup>1,2</sup>, Remco van de Beek<sup>2</sup>, Jafet C.M. Andersson<sup>2</sup>,  
5 Hossein Hashemi<sup>1</sup>, Jonas Olsson<sup>1,2</sup>

6 <sup>1</sup> Division of Water Resources Engineering, Faculty of Engineering, Lund University, P.O. Box  
7 118, 22100 Lund, Sweden

8 <sup>2</sup> Swedish Meteorological and Hydrological Institute (SMHI), Folkborgsvägen 17, Norrköping  
9 SE-601 76, Sweden

10 \*Corresponding author. E-mail: louise.petersson\_wardh@tvrl.lth.se.

## 11 Abstract

12 Short-duration extreme rainfall can cause severe impacts in built environments and flood  
13 mitigation measures require high-resolution rainfall data to be effective. It is a particular  
14 challenge to observe convective storms, which are expected to intensify with climate change.  
15 However, rainfall monitoring networks operated by national meteorological and hydrological  
16 services generally have limited ability to observe rainfall at sub-hourly and sub-kilometre  
17 scales. This paper investigates the capability of second- and third-party rainfall sensors to  
18 observe a highly localized convective storm that hit southwestern Sweden in August 2022.  
19 Specifically, we compared the observations from professional weather stations, C-band radar,  
20 X-band radar, Commercial Microwave Links and Personal Weather Stations to get a full  
21 impression of the sensors' strengths and weaknesses in the context of convective storms. The  
22 results suggest that second- and third-party networks can contribute important information on  
23 short-duration extreme rainfall to national weather services. The second-party network  
24 assisted in quantifying the magnitude and spatial variability of the event with high accuracy.  
25 The third-party network could contribute to the understanding of the duration and spatial  
26 distribution of the storm, but it underestimated the magnitude compared with the reference  
27 sensors.

## 28 1. Introduction

29 The global trend of urbanization is increasingly exposing people and assets to flood risks,  
30 which particularly affects the urban poor (Winsemius et al., 2018; Petersson et al., 2020; UN-  
31 Habitat, 2024). Flood mitigation and disaster preparedness measures require rainfall  
32 measurements on sub-hourly and sub-kilometre scales to be effective from the planning phase  
33 to post-event analysis (Guo, 2006; Marchi et al., 2009; Mailhot and Duchesne, 2010; Fuentes-

Formatted: English (United States)

Formatted: English (United States)

34 Andino et al., 2017; Pulkkinen et al., 2019; Imhoff et al., 2020). However, traditional monitoring  
35 techniques generally have limited ability to accurately observe rainfall at this spatiotemporal  
36 resolution. The most impactful rainfall events in urban areas are typically convective storms,  
37 which can cause heavy rain over small areas and short durations with severe damage as a  
38 consequence (Kaiser et al., 2021; Mobini et al., 2021).

Formatted: English (United States)

39 In Sweden, the Swedish Meteorological and Hydrological Institute (SMHI) operates around  
40 600 rain gauges across a landmass of 410,000 km<sup>2</sup>. Of these, around 130 are automatic  
41 stations recording accumulated rainfall depth every 15 minutes, and the remaining are manual  
42 stations reporting daily amounts. The station network is complemented with 12 C-band  
43 Weather Radars (CWR) across the country with outputs every 5 minutes at 2 km spatial  
44 resolution. While CWR generally is capable of producing a good spatial representation of  
45 precipitation, it has limitations caused by beam overshooting, beam blockage and clutter (van  
46 de Beek et al., 2016; Einfalt et al., 2004). For highly localized convective events, the  
47 spatiotemporal resolution of Sweden's official gauge network and radar composite is too low  
48 to capture essential rainfall dynamics, such as spatial variability and peak intensity.

Formatted: English (United States)

49 One option for national meteorological and hydrological services (NMHS) to access high-  
50 resolution rainfall measurements is to reach agreements with other professional entities like  
51 municipal water utilities and universities that maintain their own monitoring networks, so-called  
52 "second-party data" (Garcia-Marti et al., 2023). While these data might be trustworthy for  
53 operational use, their sampling resolution may, just like official data, be insufficient on the  
54 "unresolved spatial scale" in which convective storms occur (Lussana et al., 2023) (Lussana  
55 et al., 2023). In light of this, SMHI has recently gained interest in additional external  
56 observations not operated by any official agency, sometimes referred to as "third-party data".  
57 The new technologies are often enabled by digitalization and user-generated content on the  
58 Internet, which lowers the barriers and costs associated with data acquisition. While these data  
59 can provide higher resolution observations in space and time, they are often subject to  
60 uncertainties and bias due to the lack of installation guidelines, maintenance protocols and  
61 mechanisms to reinforce such standards. These promises and concerns have sparked  
62 research efforts on applications and quality control of third-party data at SMHI and many other  
63 European NMHS (Hahn et al., 2022; Garcia-Marti et al., 2023).

Formatted: English (United States)

64 This paper investigates the capability of second- and third-party rainfall sensors to observe a  
65 highly localized convective storm that occurred on 18 August 2022 in Båstad, Sweden. The  
66 second-party data comes from sensors managed by local authorities in Skåne County and  
67 consists of a traditional rain gauge and an X-band Weather Radar (XWR). As for third-party  
68 data, we study rainfall observations from a Commercial Microwave Link (CML) and a set of  
69 Personal Weather Stations (PWS). CML and PWS are sometimes referred to as "opportunistic

70 sensors" (Fencl et al., 2024). Here, we will use the term "third-party data" for consistency. First,  
71 the long-term (2021-2022) performance of the second-party rain gauge is evaluated against  
72 the national weather stations to qualify as a trusted reference sensor for the study. Then, an  
73 event analysis is performed by calculating evaluation metrics for each sensor compared with  
74 the reference. Data from the radars and third-party sensors require pre-processing and quality  
75 control to facilitate the analysis.

Formatted: English (United States)

76 XWRs are lower-cost compared with conventional C-band and S-band weather radars and  
77 provide higher resolution imagery. They are, on the other hand, more affected by attenuation,  
78 especially in widespread heavy rainfalls due to the accumulated attenuation throughout the  
79 signal path (Lengfeld et al., 2016; Bobotová et al., 2022). XWRs also have a shorter  
80 observation range than conventional radars, typically 30-60 km (Thorndahl et al., 2017).

Formatted: English (United States)

Formatted: English (United States)

81 CMLs are radio links between base stations that connect the backbone of telecom networks  
82 to local subnetworks (Chwala and Kunstmann, 2019). CMLs operate at frequencies where the  
83 propagation of radio waves through the atmosphere is attenuated by rainfall. The transmitted  
84 signal level (TSL) and received signal level (RSL) are collected by telecom companies for  
85 network monitoring and maintenance purposes, so what is being considered as "noise" in  
86 telecommunication can be used as a signal to estimate rainfall intensities for  
87 hydrometeorological applications (Leijnse et al., 2007b). In this paper we study the spatial  
88 variability of rainfall along a CML link by sampling XWR bins every 250 meters along the CML  
89 reach, resulting in 20 XWR time series that are compared with the CML rainfall estimates. This  
90 approach enables us to perform detailed investigations about bias in CML observations due to  
91 the variability of rainfall intensity along a CML path.

Formatted: English (United States)

Formatted: English (United States)

92 PWS are weather stations installed by people on their private property. Here, we consider  
93 PWS that can be connected to online platforms to share observations openly in real time.  
94 Recent years have seen a remarkable increase in PWS connected to the internet, presumably  
95 due to the adoption of smart home technologies (Sovacool and Furszyfer Del Rio, 2020).  
96 Contrary to CML, PWS are designed to measure rainfall directly, but it can be assumed that  
97 PWS data are subject to errors and bias linked to hardware, installation site and maintenance  
98 (Boonstra, 2024). Various quality control protocols explicitly designed for PWS have been  
99 presented in the literature (de Vos et al., 2019; Bárdossy et al., 2021; Lewis et al., 2021).  
100 However, it has not been investigated how the algorithms perform when applied to localized  
101 extreme rainfall. In this paper, we apply an adjusted version of the PWS quality control protocol  
102 suggested by de Vos et al. (2019) and compare the results with traditional evaluation metrics.

Formatted: English (United States)

Formatted: English (United States)

Field Code Changed

Formatted: English (United States)

103 This paper addresses multiple gaps in high-resolution monitoring of convective rainfall by  
104 bench-marking second- and third-party sensors with an official monitoring network, and by

105 investigating the performance of a PWS quality control protocol in this context. The study is  
106 guided by an ambition to contribute to answering the following general research questions:

- 107 • To what extent are second- and third-party sensors capable of observing convective  
108 rainfall?
- 109 • What are the advantages and limitations of observing convective rainfall with second-  
110 and third-party sensors, compared with a national monitoring network?

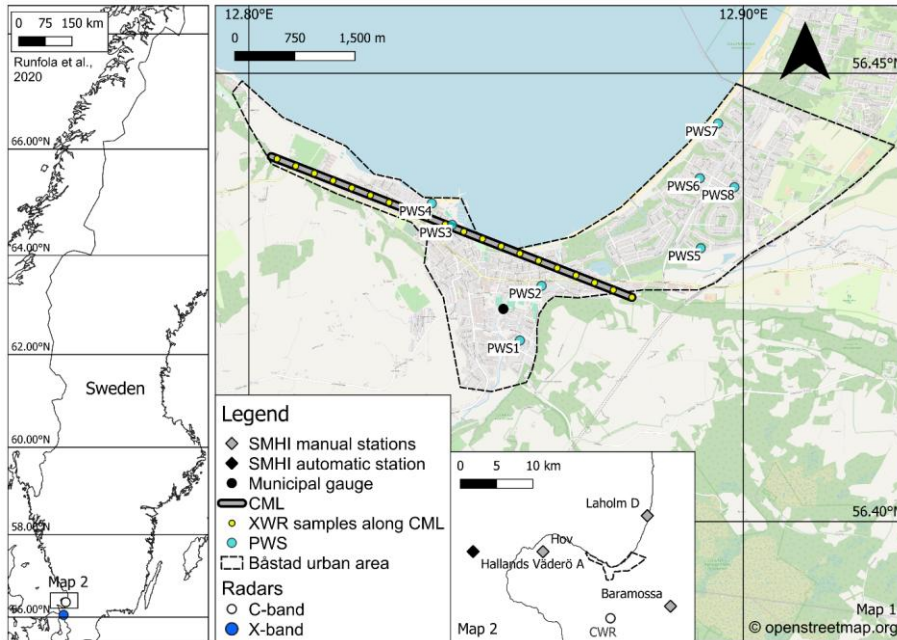
111 This paper is organized as follows. After this introductory section, Section 2 presents the storm  
112 event and area of interest that was selected for the case study. Section 3 describes the sensors  
113 and data applied in the analysis. Section 4 presents evaluation metrics and methods applied  
114 for the long-term and event analysis. Section 5 outlines the results of the long-term and event  
115 analysis. Section 6 discusses the results, while Section 7 summarizes the main findings of the  
116 study.

## 117 2. Case study

118 A convective rainfall event that hit the Bjäre Peninsula in Skåne County, Sweden, in the late  
119 afternoon of 18 August 2022, was selected for the study. SMHI's forecast had indicated a small  
120 likelihood of rainfall intensities above 35 mm/3h, which is the institute's threshold for rainfall  
121 weather warnings. However, it was expected to hit further to the north, so no weather warning  
122 was issued in the area at the time of the event. According to media reports, the rain was mixed  
123 with hailstones of about 2 cm in diameter and caused flooding of around 60 buildings  
124 (Gravlund, 2025; Bengtsson, 2023). A local water utility company (NSVA) operates a tipping  
125 bucket rain gauge (hereafter 'municipal gauge') in the city of Båstad, which peaked at 216  
126 mm/h and recorded 75.4 mm in 64 minutes. This corresponds to a return period of about 700  
127 years, based on rainfall statistics developed for southwestern Sweden (Olsson et al., 2019).  
128 The maximum depth recorded in 45 minutes was 71.2 mm, which breaks Sweden's official  
129 record of 61.1 mm in 45 minutes at the *Daglösen* station in Värmland County on 5 July 2000.  
130 The predominant wind direction in the area is from the southwest to the northeast, and the  
131 selected event was preceded by two dry days. The analysis focused on the urban area of  
132 Båstad, a town with around 16,000 inhabitants located on the southern coast of the Laholm  
133 Bay, covering approximately 9.4 km<sup>2</sup>. Fig. 1 shows the locations of all sensors included in the  
134 study.

Formatted: English (United States)

135



136

137 **Figure 1.** Area of interest and locations of sensors.

### 138 3. Data

139 Three levels of data were considered in the study – Sweden’s national meteorological  
140 monitoring network, a municipal gauge and XWR operated by local and regional agencies  
141 (second-party network) and CML and PWS (third-party network). More details on the data  
142 sets are provided below.

#### 143 3.1 National monitoring network

144 The national weather monitoring network operated by SMHI consists of a combination of  
145 manual and automatic weather stations and CWR. The *Hov*, *Laholm D* and *Baramossa*  
146 weather stations, located 9-10 km away from Båstad (Fig. 1), report daily accumulated rainfall  
147 at 06:00 UTC+2, manually observed by certified observers. The automatic rain gauge  
148 of weighing type on the island *Hallands Väderö*, situated 15 km west of Båstad, reports 15-  
149 minute accumulations. As these data have passed quality assurance protocols at SMHI, we  
150 consider them the most trustworthy source to use for benchmarking in the study. Precipitation  
151 data from the stations for the year 2022 were downloaded from SMHI’s open data archive  
152 (SMHI, 2025b).

153 In addition, we studied a gauge-adjusted Plan Position Indicator (PPI) horizontal reflectivity  
 154 composite based on the lowest elevation scan (0.5°) from all radars operated by SMHI. The  
 155 composite is used operationally for weather forecasting at the institute. The composite is  
 156 available in 5-minute resolution at a spatial resolution of 2x2 km and distributed as radar  
 157 reflectivity data in SMHI's open radar archive (SMHI, 2025c). The gauge-adjustment technique  
 158 is based on the gauge-to-radar ratio and is targeted towards real-time applications (refer to  
 159 Michelson & Koistinen (2000), for details). Radar data compositing at SMHI is performed using  
 160 the *BALTRAD* software (Michelson et al., 2018) (Anon, n.d.). While the radars can operate in  
 161 dual-polarization mode, this product is based on the horizontal polarization. The closest radar  
 162 (radar location *Ångelholm*) is situated 6 km south of Båstad, (Fig. 1, map 2). Since this radar  
 163 was operational during the selected event and the compositing method is based on the closest  
 164 radar, the studied composite is based on data from only this radar during the period of interest.  
 165 Radar reflectivity  $Z$  [ $\text{mm}^6/\text{m}^3$ ] can be expressed as integrals over the Drop Size Distribution  
 166 (DSD) in the pulse volume, here  $N(D)$  [ $\text{mm}/\text{m}^3$ ].

$$Z = \int_0^{\infty} D^6 N(D) dD \quad (1)$$

167 where  $D$  [mm] is the spherical drop diameter. It is generally expressed logarithmically as *dBZ*:

$$dBZ = 10 \times \log_{10}(Z) \quad (2)$$

168 The CWR composite retrieved from SMHI's radar archive is distributed as pseudo-dBZ  $E$   
 169 (integer 0-255) to enable a smaller storage size, following European standards (Michelson et  
 170 al., 2014). To convert these integers back to *dBZ*, gain  $G$  and offset were applied:

$$dBZ = E \times G + offset \quad (3)$$

171 where  $G = 0.4$  and  $offset = -30$  (Michelson et al., 2014). The rain rate  $P_{CWR}$  (mm/h) can be  
 172 found from the reflectivity following an inverted power law relationship:

$$P_{CWR} = \left(\frac{Z}{a}\right)^{\frac{1}{b}} \quad (4)$$

173 We applied the parameters suggested by Marshall & Palmer (1948) (1948),  $a=200$  and  $b=1.6$ .  
 174 The actual values of  $a$  and  $b$  can vary greatly depending on the actual DSD, which may be  
 175 different within and from event to event (Battan, 1973). CWR time series at a 5-minute  
 176 resolution were sampled at the locations of the municipal rain gauge and the eight PWS.

177 Figure 2 shows the elevation profile and radar beam profile between the CWR location and the  
 178 location of the municipal gauge in Båstad. The low elevation angle and short distance to the

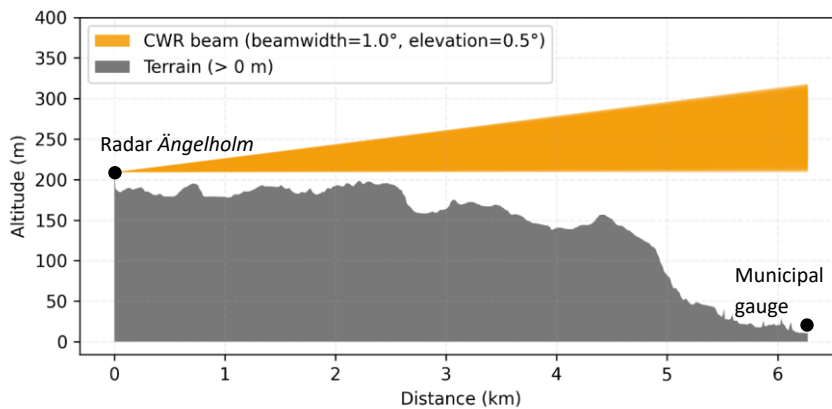
Formatted: English (United States)

Formatted: English (United States)

Formatted: English (United States)

Formatted: English (United States)

179 area of interest indicate that the observations are made at approximately 200-300 m above  
 180 sea level, eliminating the risk of beam overshooting, as convective precipitation in the summer  
 181 months typically originates from much higher altitudes. Overshooting is a common error in  
 182 radar data that appears when the radar beam shoots above the precipitation cloud (Battan,  
 183 1973; Seo et al., 2000). However, the *Ängelholm* radar is affected by partial beam blockage in  
 184 a circular sector of around 60 degrees to the north of the radar location, which covers the area  
 185 of interest (Appendix A1., Fig. A1). This is caused by vegetation within 1 km north of the radar  
 186 location (Appendix A1., Fig. A2). Evaluations at SMHI have shown that the *Ängelholm* radar  
 187 underestimated the accumulated rainfall depth of the years 2022-2023 by around 80% in the  
 188 affected area, compared with SMHI's weather stations.



189 **Figure 2.** Elevation profile and beam profile between the CWR radar location and the municipal  
 190 gauge.  
 191

### 192 3.2 Second-party monitoring network

193 We consider two second-party sensors operated by local and regional authorities: a municipal  
 194 gauge in Båstad managed by the local water utility company NSVA, and a compact FURUNO  
 195 dual-polarization XWR operated by NSVA on behalf of Lund University. The municipal gauge  
 196 is a Casella tipping bucket, which records a tip each time the bucket volume (0.2 mm) is filled  
 197 on a 1-second resolution. Time series with 1-minute resolution from the municipal rain gauge  
 198 for the years 2021-2022 were received upon request from NSVA.

199 About 80% of Skåne County is covered by observations from two XWRs located in Dalby and  
 200 Helsingborg (Hosseini et al., 2023). In this study, we used data from the XWR in Helsingborg,  
 201 40 km south of Båstad (Fig. 1). The spatial resolution of the data is 0.5 degrees of azimuth and  
 202 75 m of slant range. XWR data for the day of the event was acquired from VeVa (*Weather*  
 203 *Radar in the Water Sector*) (Foreningen VeVa – Vejrradar i vandsektoren, 2025), a

Formatted: English (United States)

Formatted: English (United States)

204 collaboration between water utility companies in south Sweden and Denmark that distributes  
205 XWR data to its partners according to the EUMETNET Opera Data Information Model  
206 (Michelson et al., 2014).

Formatted: English (United States)

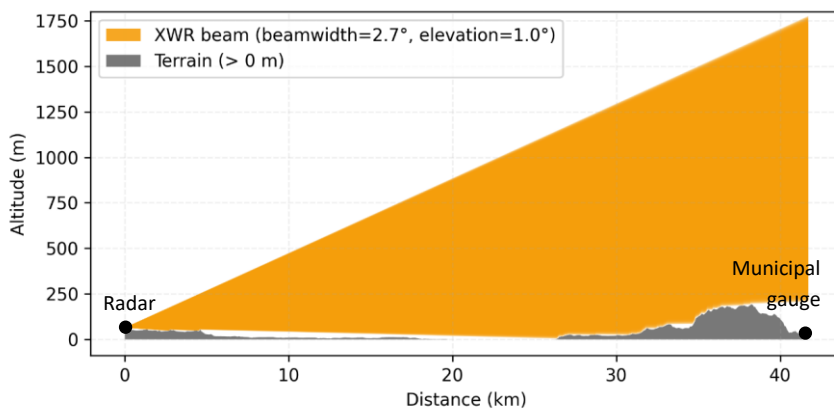
207 The manufacturer's built-in precalculated rainfall rate  $P_{XWR}$  (mm/h) from the lowest scan  
208 (elevation angle of  $1^\circ$ ) on 1-minute resolution was used for the study. The underlying equations  
209 for calculating the rainfall rate are generally similar to CWR as described in Section 3.1.  
210 However, a main difference is that the XWR data integrates dual-polarization variables as a  
211 method for attenuation correction, as described in detail in Hosseini et al. (2020). This method  
212 estimates attenuation as an approximately linear function of the specific differential phase shift,  
213 which depends on phase rather than signal intensity and is therefore less sensitive to  
214 attenuation (Kumjian, 2013). The method has been shown to be useful for summer  
215 precipitation estimations in Sweden (Hosseini et al., 2023).

Formatted: English (United States)

Formatted: English (United States)

Formatted: English (United States)

216 Figure 3 shows that the XWR's beamwidth has a much larger sampling volume and steeper  
217 elevation angle than CWR (Fig. 2) at the area of interest, which suggests a small risk of signal  
218 contamination due to beam blockage. As the profile extends 250-1750 meters above sea level  
219 over Båstad, this, just like for CWR, suggests a small risk of beam overshooting.



220  
221 **Figure 3.** Elevation profile and beamwidth between the XWR radar location and the municipal gauge.

### 222 3.3 Third-party monitoring network

223 Two types of third-party sensors were included in the study – CML and PWS. The location of  
224 the only CML in the area of interest is shown in Fig. 1. This link is approximately 4.8 km long  
225 and has a frequency of 23.1 GHz. CML data were received as TSL and RSL at 10-second  
226 resolution upon request from the telecom companies Ericsson AB and Tre. The data covered

227 all base stations on the Bjäre Peninsula for the days 18-19 August 2022. Each antenna  
228 works as both a transmitting and receiving terminal, meaning that each link has bidirectional  
229 transmission and provides at least two radio signals. Here, we use the term ‘sub-link’ to refer  
230 to a single radio signal.

231 Received TSL and RSL were converted into rainfall rate using the MEMO (Microwave-based  
232 Environmental Monitoring) method developed by SMHI (MEMO, 2025). This method follows  
233 the general steps applied by most CML algorithms as described in Appendix A2. However, the  
234 process does not explicitly correct for wet antenna attenuation, but instead applies a bias  
235 correction factor  $CF_A$  based on link length to the derived rain rate  $P_{raw}$  (mm/h) that compensates  
236 for the wet antenna effect:

$$P_{CML} = P_{raw} - (A_{nl} * CF_A) \quad (5)$$

237 Here,  $P_{raw}$  is the uncorrected rainfall intensity and  $A_{nl}$  is the net attenuation. More details on  
238 CML processing are found in Appendix A2.

239 The selected PWS type in this study, NetAtmo, is an unheated plastic tipping bucket rain  
240 gauge that reports the number of tips through a wireless connection to the accompanying  
241 indoor module (de Vos et al., 2019). The indoor module broadcasts the observations to  
242 Netatmo’s online platform at approximately 5-minute intervals. The default tipping bucket  
243 volume is 0.101 mm, or another volume specified by the station owner using the product’s  
244 calibration feature. PWS time series for the study were received from NetAtmo. PWS without  
245 a rainfall sensor, and PWS that were offline during the storm event, were excluded from the  
246 analysis. This resulted in a total of eight PWS located within the Båstad urban area (Fig. 1).  
247 The PWS data were quality controlled as described in Section 4.4.

## 248 4. Methods

249 The analyses covered two stages – a long-term analysis and an event analysis. This section  
250 first presents the evaluation metrics applied to assess the performance of the sensors in the  
251 study, followed by descriptions of the methods applied in the long-term analysis and event  
252 analysis. Then, the quality control of PWS data is described, as well as time lags applied to  
253 the radar data.

### 254 4.1 Evaluation metrics

255 Three evaluation metrics were used to assess the performance of each sensor: Spearman’s  
256 rank correlation ( $r_s$ ), Root Mean Squared Error (RMSE), and Percent Bias (PBIAS). The  
257 metrics were calculated on different temporal resolutions in different analyses, see Sections  
258 4.2 and 4.3. For each analysis, the metrics were calculated for the duration of the event as  
259 recorded by the respective reference sensor, see Section 4.3.

Formatted: English (United States)

Formatted: English (United States)

260 The Spearman correlation is a non-parametric test that measures the strength of a monotonic  
261 relationship between two variables:

$$r_s = 1 - \frac{6 \sum d_i^2}{n(n^2 - 1)} \quad (6)$$

263 where  $d_i$  is the difference between ranks for each pair of values and  $n$  is the number of  
264 observations. The closer to -1 or 1, the better the negative or positive monotonic relationship.  
265 As the Spearman correlation does not address the magnitude of error, it can be complemented  
266 with RMSE (Hyndman and Koehler, 2006):

$$RMSE = \sqrt{\frac{1}{n} \sum_{i=1}^n (O_i - T_i)^2} \quad (7)$$

268 where  $O_i$  is the reference rainfall and  $T_i$  is the evaluated data. Lower RMSE indicates a better  
269 model performance. Finally, PBIAS quantifies the average bias, where a positive or negative  
270 value suggests an underestimation or overestimation of rainfall depth, respectively (Gupta et  
271 al., 1999):

$$PBIAS = 100 \times \frac{\sum_{i=1}^n (O_i - T_i)}{\sum_{i=1}^n O_i} \quad (8)$$

## 273 4.2 Long-term analysis

274 As the magnitude of the selected event was not captured by the national network (see Results)  
275 it was necessary to establish another reliable reference for the event analysis. Consequently,  
276 the long-term (2021-2022) performance of the municipal gauge was evaluated against the  
277 national weather stations using the metrics presented in Section 0.1 at daily resolution. The  
278 gauge was cross-referenced with the manual stations *Hov*, *Laholm D* and *Baramossa* operated  
279 by SMHI, all situated 9.3-9.7 km away (Fig. 1). The station *Hallands Väderö A* was excluded  
280 from the comparison as it is located on an island 15 km west of Båstad. The tips recorded by  
281 the municipal gauge were resampled to daily accumulations between 06:00-05:59 UTC+2, as  
282 this is the sampling frequency of the reference (manual) stations.

## 283 4.3 Event analysis

284 The temporal range of the studied event differed between each sensor, as the start and end  
285 of the rainfall occurred at different times in the observed time series. The reference used for  
286 each comparison is outlined below. The event start was defined as the first timestep when it  
287 had been raining more than 0.1 mm/h for at least 5 minutes at the reference sensor, and the

Formatted: English (United States)

Formatted: English (United States)

288 event stop was when it had been raining less than 0.1 mm/h for at least 5 minutes (Section  
289 5.2.1). The return period of the event was calculated based on SMHI's climate statistics for  
290 southwestern Sweden (Olsson et al., 2019). The calculation of evaluation metrics, return  
291 periods, and accumulated depths were carried out for the duration of the event as recorded  
292 by the reference sensor.

293 Based on performance, it was decided to exclude CWR as a reference (Section 5.2.2). The  
294 CWR composite was sampled at the location of the municipal gauge, and the metrics were  
295 calculated at 5-minute resolution (the resolution of the CWR data) with the municipal gauge  
296 as the reference. The accumulated rainfall  $D_{CWR}$  (mm) was then calculated at the location of  
297 the municipal gauge and for the whole CWR composite in the area of interest.

298 The XWR data were available in polar bins, that is, range gates at a given elevation and  
299 azimuthal angle, in contrast to the regular Cartesian grids for the utilized CWR data. Thus,  
300 time series were extracted from the XWR polar bin closest to the projected locations of  
301 interest, accounting for elevation, range difference, and azimuth difference. The sampled  
302 locations included the municipal gauge, the eight PWS, and 20 points along the CML path,  
303 as described below. The elevation metrics were calculated on the time XWR time series  
304 sampled at the municipal gauge on a 5-minute resolution with the municipal gauge as  
305 reference. After concluding that XWR recorded similar rainfall depth as the municipal rain  
306 gauge during the event, XWR was used as a reference for CML and PWS to better account  
307 for the spatial variability of the rainfall. For visualization purposes, the volumetric XWR data  
308 was gridded into a Cartesian grid of 500250-meter resolution using ~~the wradlib Python~~  
309 ~~package (Mühlbauer & Heistermann, 2024)~~ [linear interpolation with Delaunay triangulation](#).

310 The accumulated rainfall  $D_{XWR}$  (mm) was calculated for the whole area of interest based on  
311 the gridded data.

312 A few missing values were found in the XWR time series, which occurred during the most  
313 intense part of the storm. Investigations showed that these bins likely observed rainfall  
314 intensities above 255 mm/h, which is the upper limit for storing integers in 8-bit format and  
315 which was used by VeVa when calculating the rain rate. The missing values were filled with  
316 temporal linear interpolation.

317 The CML included in this study consists of two sub-links. These recorded similar values, with  
318 a difference in total rainfall depth of around 5% for the whole event. Thus, the mean rain rate  
319  $P_{CML}$  and mean depth  $D_{CML}$  per timestep of the two sub-links were used in the analysis. The  
320 XWR polar bins data were sampled every 250 m (20 points, Fig. 1) along the reach of the  
321 CML to investigate the variability of rainfall intensity along the link, resulting in 20 XWR time

Formatted: English (United States)

Formatted: English (United States)

322 series on 1-minute resolution. Evaluation metrics were calculated on 1-minute resolution with  
323 the mean of 20 XWR samples,  $\bar{P}_{XWR}$ , as reference.

324 To investigate how CML estimates of extreme rainfall are impacted by spatial variability along  
325 the link, the 10<sup>th</sup> and 90<sup>th</sup> percentiles were calculated to explore the range of  $P_{XWR}$  and  $D_{XWR}$   
326 along the CML path. The behavior of the XWR data along the CML during the intense part of  
327 the storm was inspected visually. Hypothesizing that the difference in XWR and CML  
328 observations is related to the XWR variability along the link, an ordinary least squares analysis  
329 was performed on the difference  $\bar{P}_{XWR}$  and  $\bar{P}_{CML}$ , with the XWR standard deviation as the  
330 independent variable.

331 For each PWS, the evaluation metrics were calculated compared with the XWR time series  
332 sampled at the PWS location on 5-minute resolution. The PWS timeseries were processed  
333 with a quality control package as described below.

#### 334 4.4 PWS Quality Control

335 Research has shown that the quality of rainfall data from PWS can be improved significantly  
336 by applying quality control and bias correction. The algorithms suggested in literature, e.g.  
337 Mandement & Caumont (2020), Lewis et al. (2021), Bárdossy et al. (2021), typically utilize the  
338 high observation density of PWS by comparing rainfall time series with the performance of  
339 neighboring stations, referred to as 'buddy checks' by Báserud et al. (2020). De Vos et al.  
340 (2019) developed a quality control protocol for PWS rainfall data in the R programming  
341 language, PWSQC. The method does not rely on a primary monitoring network, but flags  
342 suspicious measurements based on the observations from nearby stations. The method has  
343 been applied in gauge-adjustment of radar by Nielsen et al. (2024) and Overeem et al. (2024)  
344 and has recently been converted to a Python package, *pypwsqc*, that was applied for the study  
345 (Graf et al., 2025)(Chwala et al., n.d.).

346 Event time series from the eight PWS were processed with *pypwsqc*. The algorithm applies  
347 three filters utilizing neighbor checks – the Faulty Zeroes filter, High Influx filter, and Station  
348 Outlier filter – to assess the quality of each time step in rainfall time series by comparing with  
349 the records of neighboring PWS within a user-defined radius (refer to de Vos et al., 2019, for  
350 details). The Faulty Zeroes filter flags timesteps when the evaluated station records zero  
351 rainfall for at least  $n_{int}$  time intervals, while the median of the surrounding rainfall observations  
352 is larger than zero. The High Influx filter identifies unrealistically high rainfall amounts based  
353 on a comparison with the median rainfall of the neighboring stations. The Station Outlier filter  
354 flags a station as an "outlier" if the Pearson correlation with the median rainfall of neighbors in  
355 a selected evaluation period falls below a set threshold.

Formatted: English (United States)

Formatted: English (United States)

Formatted: English (United States)

Formatted: English (United States)

Field Code Changed

Formatted: English (United States)

Formatted: English (United States)

356 To improve the performance of the neighboring checks, data from all PWS within a 10 km  
357 radius around Båstad were considered, which resulted in a total of 58 stations. However, only  
358 the results of the 8 PWS within the area of interest were evaluated during the event. To get a  
359 better understanding of the long-term performance of each PWS, the quality control was also  
360 applied for the full year of 2022. The parameters were set to the same values as in the original  
361 publication (de Vos et al., 2019), except  $m_{match}$  and  $m_{int}$ . These parameters control how many  
362 wet time steps at the evaluated PWS that must be overlapping with wet time steps at the  
363 neighboring stations within a defined evaluation period to reliably apply the Station Outlier filter.  
364 The numbers proposed by de Vos et al. (2019) were found to be too strict for the PWS dataset  
365 in this study, as the Station Outlier filter could not be applied for very long periods, including  
366 during the studied storm event. Instead,  $m_{match}$  and  $m_{int}$  were set to 100 and 8064, respectively,  
367 to require less wet time steps during a longer evaluation period.

Formatted: English (United States)

Formatted: English (United States)

#### 368 4.5 Time lags

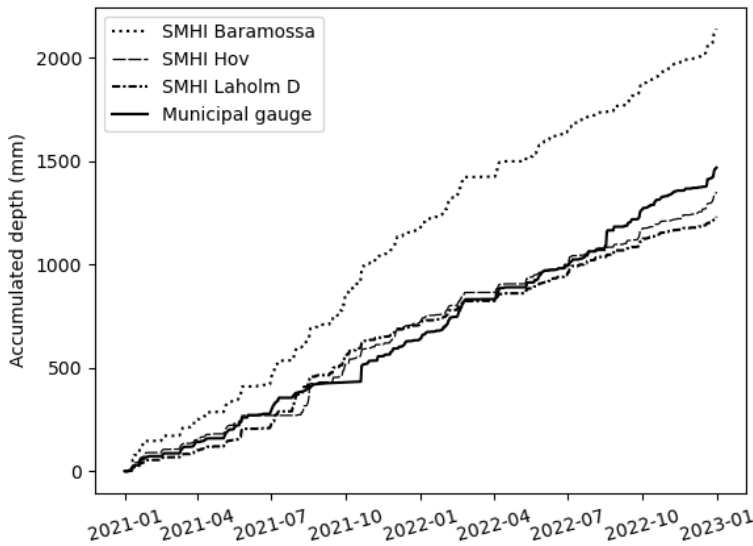
369 The event analysis revealed low correlations ( $r_s$ ) between the radars (CWR and XWR) and  
370 the reference (municipal gauge), see Sections 5.2.2 and 5.2.3. As convective rainfall is highly  
371 variable in space and time, the observations per time step can be very different at nearby  
372 locations, which can lead to low correlations even between high-quality observations.  
373 Therefore, time lags were applied to the radar time series to see if this could increase the  
374 correlation. The radar time series sampled at the municipal gauge were shifted from -10 to  
375 +10 timesteps on a 5-minute resolution. For each lag, the correlation  $r_s$  with the municipal  
376 gauge was calculated over the event duration as defined by the reference. The highest  
377 correlation value was then reported.

## 378 4. Results

### 379 5.1 Long-term analysis

380 Figure 4 shows daily accumulations from the *Hov*, *Laholm D* and *Baramossa* weather stations  
381 and the municipal gauge for the years 2021 and 2022. The plot shows that the municipal gauge  
382 recorded significantly less rainfall than *Baramossa* but followed *Hov* and *Laholm D* reasonably  
383 well. These findings align with rainfall observations of the region in the period 1991-2020  
384 (SMHI, 2025d). The inland regions of southwestern Sweden, including the northern parts of

385 Skåne County where *Baramossa* is located, overall receives more precipitation than the  
 386 coastal area, where the Båstad, Hov and Laholm stations are located.



387  
 388 **Figure 4.** Accumulated depth 2021-2022 for municipal gauge and SMHI rain gauges located 9.3-9.7 km  
 389 away.

390 Table 1 shows the evaluation metrics of the municipal gauge, benchmarked with the three  
 391 reference stations. The PBIAS over 2 years was only -8% compared with *Hov* weather  
 392 station, which is considered low as the stations are situated 9.7 km apart. Based on these  
 393 results, the municipal gauge was accepted as a trusted reference for the event analysis.

394 **Table 1.** Cross-validation of the municipal gauge with three reference stations, 2021-2022.

Reference station (SMHI)	Distance to municipal gauge (km)	$r_s$	RMSE (mm/day)	Accumulated difference (mm)	PBIAS (%)
Baramossa	9.4	0.55	6.1	674	-31%
Hov	9.7	0.46	5.87	-118	8%
Laholm	9.3	0.52	5.23	-233	19%

395  
 396 **5.2 Event analysis**

397 **5.2.1 Event duration**

398 Table 2 summarizes the event duration observed by each sensor. National weather stations  
 399 were excluded from the analysis, either because they record daily precipitation, or because

400 they recorded very small total depth (Section 4.2.2). The municipal gauge recorded rainfall  
 401 for 64 minutes, which is among the shortest durations with only PWS 4 observing rain for a  
 402 shorter period (50 min). Notably, XWR recorded rain for 109 minutes at the location of the  
 403 municipal gauge. This follows the general pattern that XWR recorded rain for a longer period  
 404 than the corresponding gauge. The difference was generally around 30 minutes, possibly  
 405 due to the higher sensitivity of XWR to light drizzles, either never reaching the ground or  
 406 slowly accumulating in the tipping bucket before the first tip was recorded at the weather  
 407 station. Comparing XWR with CML, there was only 4 minutes difference in the observed  
 408 event start.

409 The PWS are concentrated in two clusters. PWS 1-4 are located in the western and central  
 410 part of Båstad together with the municipal gauge, and PWS 5-8 in the north-eastern part  
 411 (Fig.1). In Table 2, it can be seen that ground observations in the mid-western part of Båstad  
 412 started recording rain between 16:55 and 17:15, and the north-eastern part between 17:15  
 413 and 17:25, which suggests a gradual motion of the storm from west/south-west to the north-  
 414 east. A similar tendency is seen in the XWR data, but with approximately 30 minutes time  
 415 lag.

416 **Table 2.** Event duration observed by each sensor.

Sensor	Type	Event start (UTC+2)	Event end (UTC+2)	Duration (min)
Municipal gauge	reference	17:05	18:09	64
XWR at municipal gauge	test	16:45	18:34	109
CWR at municipal gauge	test	16:45	17:55	70
XWR mean along CML	reference	16:38	18:36	118
CML mean	test	16:34	18:43	129
XWR at PWS 1	reference	16:40	18:30	110
PWS 1	test	17:05	18:30	85
XWR at PWS 2	reference	16:45	18:30	105
PWS 2	test	17:10	18:30	80
XWR at PWS 3	reference	16:40	18:30	110
PWS 3	test	16:55	18:10	75
XWR at PWS 4	reference	16:40	18:10	90
PWS 4	test	16:55	17:45	50
XWR at PWS 5	reference	16:45	18:35	110
PWS 5	test	17:25	20:00	155
XWR at PWS 6	reference	16:45	18:35	110
PWS 6	test	17:15	18:35	80
XWR at PWS 7	reference	16:50	18:35	105
PWS 7	test	17:25	18:35	70
XWR at PWS 8	reference	16:45	18:35	110
PWS 8	test	17:20	18:30	70

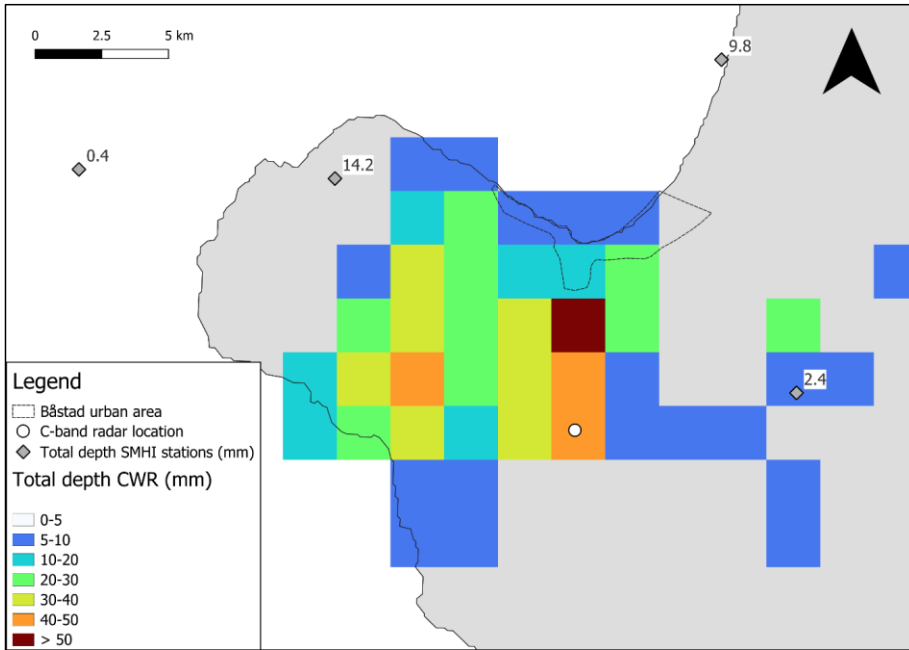
417

418 5.2.2 National monitoring network

419 The total rainfall depth observed by the national monitoring network is shown in Fig. 5. The  
420 CWR grid size is 2x2 km. The weather station *Hallands Väderö A*, situated 15 km west of  
421 Båstad, records accumulated values every 15 minutes but only observed a total volume of  
422 0.4 mm on the day of the event. The other stations report daily accumulations between  
423 06:00-05:59 UTC+2, amounting to a maximum depth of 14.2 mm at *Hov*. All observations  
424 from SMHI's gauges corresponded to a return period of less than 1 year (Olsson et al.,  
425 2019). The heaviest rainfall observed by CWR was concentrated in the south of the Båstad  
426 urban area, with a maximum total depth of 65 mm, which corresponds to a return period of  
427 around 400 years for a duration of 60 minutes (Olsson et al., 2019). The maximum recorded  
428 depth in the area of interest was 25 mm (to the south-east), which corresponds to a return  
429 period of 11 years for a duration of 60 minutes.

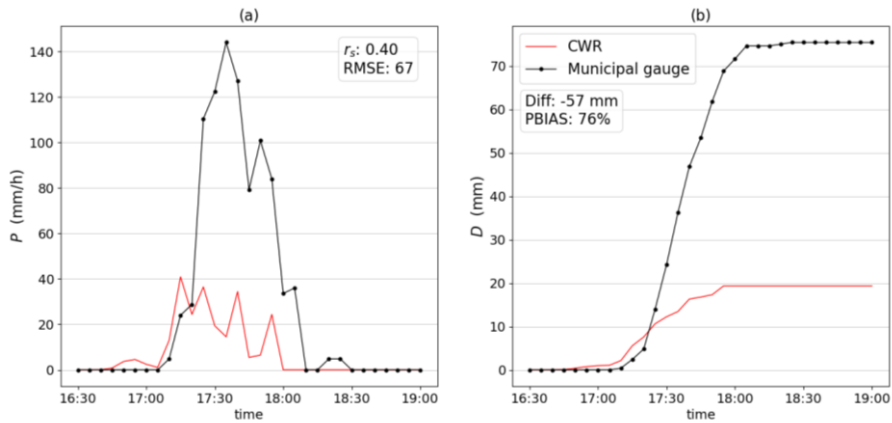
Formatted: English (United States)

Formatted: English (United States)



431 **Figure 5.** Total accumulated depth (mm) of the event recorded by the national monitoring network.

432 Figure 6 shows the rainfall event observed by the municipal gauge, compared with CWR  
433 sampled at the same location. CWR underestimated the total depth with 57 mm when  
434 compared with the gauge, which suggests that CWR could not quantify the magnitude of the  
435 event accurately. The CWR started to observe rain 20 minutes before the rain gauge. Different  
436 time lags were applied to the time series by iteration, and it was found that  $r_s$  could be raised  
437 from 0.4 to 0.83 when adding a lag of 10 minutes to the CWR data.



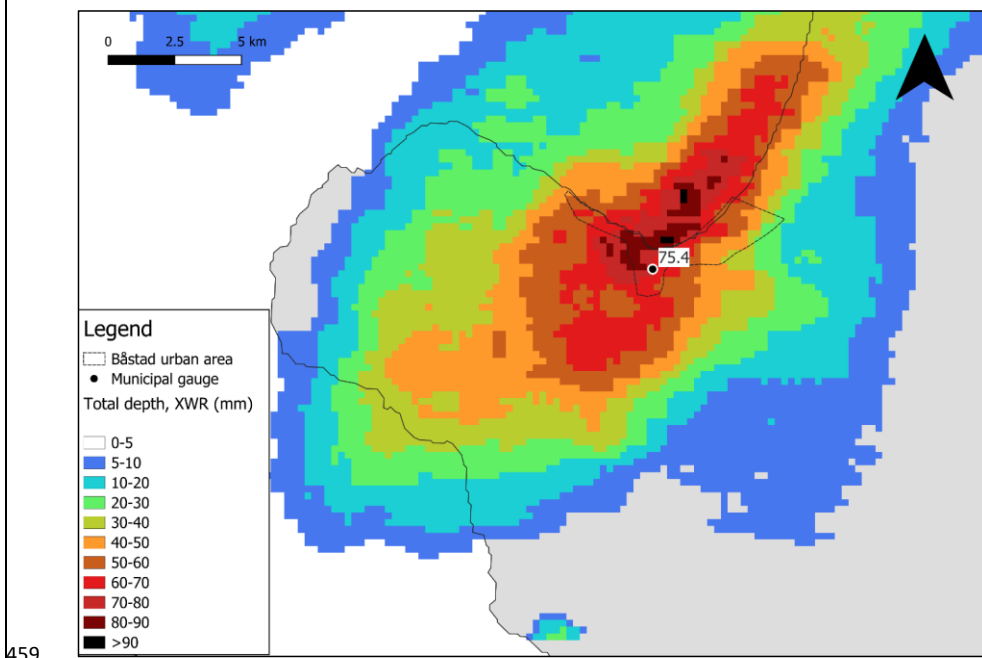
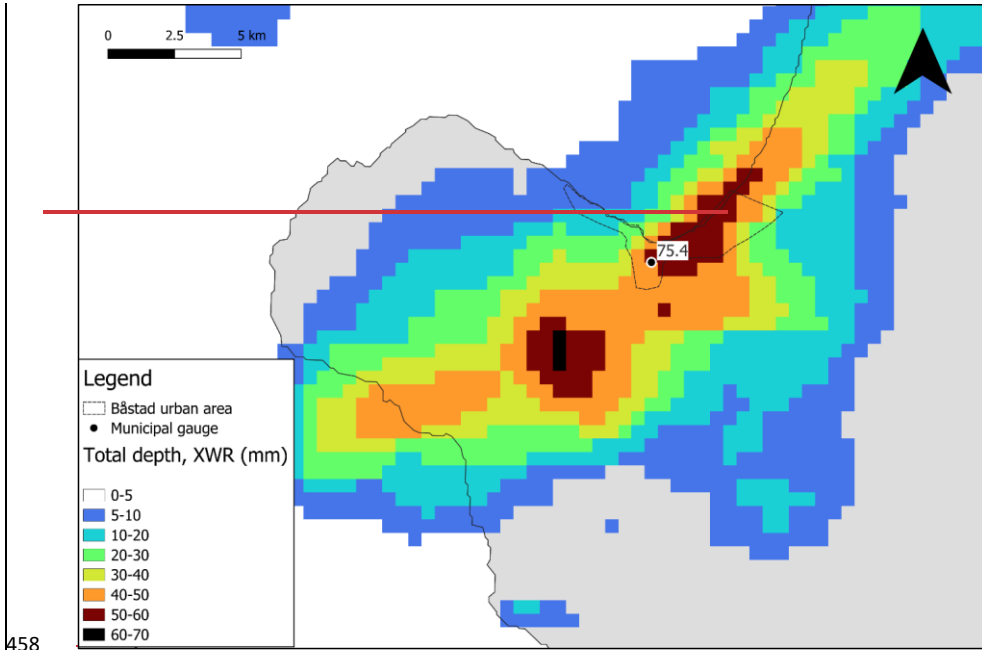
438

439 **Figure 6.** a) Rainfall intensity  $P$  (mm/h), Spearman's rank coefficient  $r_s$  (-) and RMSE (mm/h). b)  
 440 Accumulated depth  $D$  (mm), difference in total depth and PBIAS. Evaluation metrics applied on CWR  
 441 with municipal gauge as reference.

#### 442 5.2.3 Second-party monitoring network

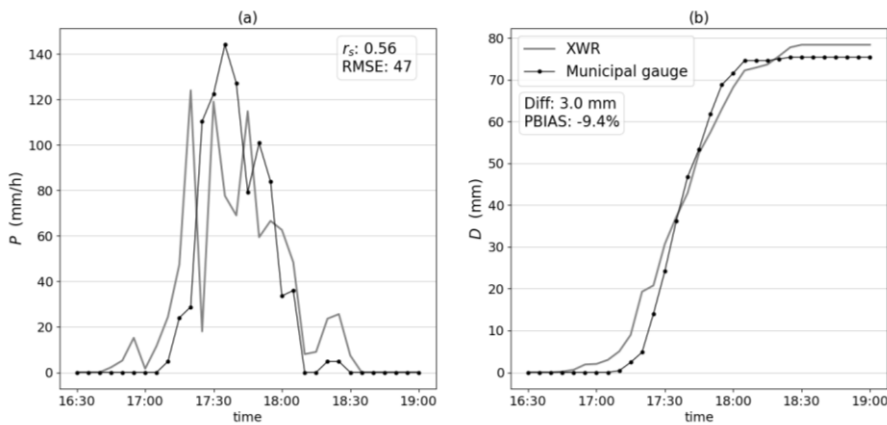
443 Figure 7 shows the total accumulated depth observed by the second-party network. The  
 444 municipal gauge observed a total depth of 75.4 mm between 17:05 and 18:09, which is here  
 445 approximated as 60 minutes. This corresponds to a return period of around 700 years (Olsson  
 446 et al., 2019). The location of the heaviest rainfall was different when comparing gridded XWR  
 447 data to the CWR composite, ~~where the XWR data indicated that the storm was centered just~~  
 448 ~~outside the coastline and not to the south of the Båstad urban area. The XWR data indicated~~  
 449 ~~two hotspots; one with total depths above 50 mm in large parts of the Båstad urban area, and~~  
 450 ~~one with a maximum depth of 61 mm 5 km south west of the city. However, the~~The total depth  
 451 of XWR sampled at the location of the municipal gauge based on the closest XWR bin was  
 452 78.4 mm, corresponding to a return period of around 800 years for 60 minutes duration, ~~with~~  
 453 ~~observations up to almost 90 mm within the area of interest. The total depth in the gridded~~  
 454 ~~XWR data was lower than the point observation because of the averaging that occurs when~~  
 455 ~~interpolating the grid.~~XWR observations above 5 mm occurred over a much larger area  
 456 compared with the CWR, especially to the north-east. This suggests that the CWR indeed was  
 457 affected by beam blockage during the event as described in Section 3.1.

Formatted: English (United States)



460 **Figure 7.** Total accumulated depth (mm) of the event recorded by the second-party monitoring network.

461 Figure 8 shows the rainfall event observed by the municipal gauge, compared with XWR polar  
 462 data sampled at the same location. As for CWR, the XWR started to record rain almost 20  
 463 minutes before the rain gauge. The correlation  $r_s$  could be raised from 0.56 to 0.7 when adding  
 464 a lag of 5 minutes to the XWR data. Even if the correlation was low with the reference, XWR  
 465 observed a similar total depth with only 3 mm overestimation. In Fig. 8a, there is a tendency  
 466 for XWR to underestimate the overall peak rainfall intensity and to overestimate lower rainfall  
 467 intensities. This might be related to signal attenuation during heavy rain and the higher  
 468 sensitivity of XWR to drizzles or observations of melting particles during light rain.

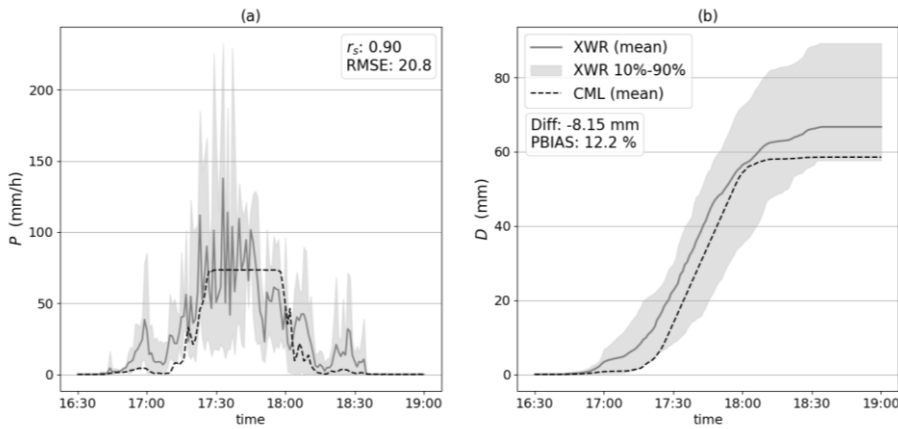


469  
 470 **Figure 8.** a) Rainfall intensity  $P$  (mm/h), Spearman's rank coefficient  $r_s$  (-) and RMSE (mm/h). b)  
 471 Accumulated depth  $D$  (mm), difference in total depth and PBIAS. Evaluation metrics applied on XWR  
 472 with municipal gauge as reference.

#### 473 5.2.4 XWR and CML analysis along the CML path

474 Figure 9 shows the rainfall intensity  $P_{CML}$  and depth  $D_{CML}$  expressed as the mean of the two  
 475 CML sub-links and the 10<sup>th</sup>-90<sup>th</sup> percentiles of the XWR bins sampled along each 250 m  
 476 (amounting to 20 sample time series) along the CML path. The mean intensity of the XWR  
 477 samples,  $\bar{P}_{XWR}$ , is highlighted in grey and was used as a reference for the CML. XWR on  
 478 average started to observe rainfall at 16:38 along the link path, and CML at 16:43.  $\bar{P}_{CML}$   
 479 reached a 'plateau' at 83 mm/h and stayed almost constant at this level for 31 minutes between  
 480 17:27-17:58. This effect is caused by the complete loss of radio signal between the CML base  
 481 stations, which is induced by the heavy rainfall, as described by Blettner et al. (2023) and Polz  
 482 et al. (2023). Likely by coincidence, CML recorded a similar total depth as the reference during  
 483 the event, leading to a relatively small PBIAS. The large spread of 10-90<sup>th</sup> percentiles obtained  
 484 from the 20 XWR observations suggests a large spatial variability of rainfall along the link.

Formatted: English (United States)

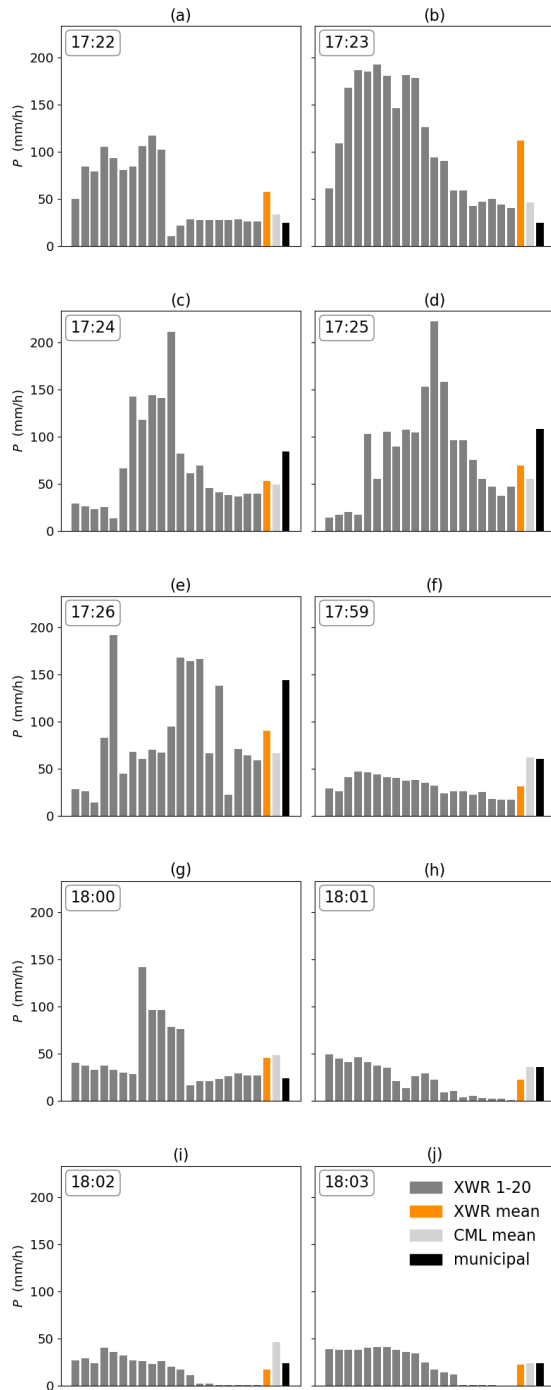


485

486 **Figure 9.** a) Rainfall intensity  $P$  (mm/h) of CML (mean) and XWR (mean and 10<sup>th</sup> to 90<sup>th</sup> percentile)  
 487 along CML path. Spearman's rank coefficient  $r_s$  (-) and RMSE (mm/h). b) Accumulated depth  $D$  (mm)  
 488 of CML (mean) and XWR (mean and 10<sup>th</sup> to 90<sup>th</sup> percentile) along CML path. Difference in total depth  
 489 and PBIAS. Evaluation metrics applied on CML mean with XWR mean as reference.

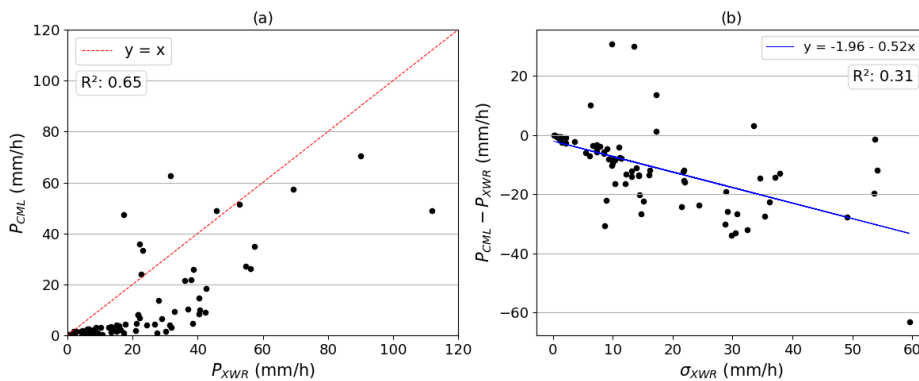
490 By inspecting radar fields, it was observed that the storm propagated almost perpendicularly  
 491 over the CML link, which is favorable for a detailed comparison between the XWR and CML  
 492 observations over the link path. Given the sudden constant records of rainfall rate observed in  
 493 the CML time series, which are clearly not representative of the actual rainfall rate, the CML  
 494 plateau period was considered unsuitable for the comparison. Instead, the following analysis  
 495 focused on the periods right before and after the signal loss, from 16:38-17:26 and 17:59-  
 496 18:36, for a total of 85 minutes.

497 Figure 10 shows the rainfall intensity distribution along the CML as observed by XWR for five  
 498 minutes before and after the plateau. The first bin to the left in the plots was sampled at the  
 499 western end of the CML, approximately 3.4 km away from the municipal gauge, and the last  
 500 bin to the right was sampled at the eastern end, 1.6 km away from the gauge (see Fig 1.). The  
 501 XWR sampling points closest to the rain gauge (bins 14 and 15, counting from the left) are at  
 502 approximately 700 meters' distance from the gauge.  $\bar{P}_{CML}$  and  $\bar{P}_{municipal}$  are also shown for each  
 503 time step. The XWR spatial distribution was sometimes rather smooth, with a gradual increase  
 504 and decrease along the link (e.g., Fig. 10b), but sometimes more intermittent, with large  
 505 differences between adjacent XWR samples (e.g., Fig. 10g). In the pre-plateau period (Fig.  
 506 10a-10e)  $\bar{P}_{CML} < \bar{P}_{XWR}$  consistently, whereas in the post-plateau period the relation was  
 507 generally the opposite (Fig. 10f-10j).



509 **Figure 10.** (a)-(e) Rainfall intensity 5 minutes before CML signal loss (17:22-17:26). (f)-(j)  
 510 Rainfall intensity 5 minutes after signal loss (17:59-18:03). Twenty radar bins sampled along  
 511 CML path every 250 meters (XWR 1-20), XWR mean, CML mean and municipal gauge.

512 The relationship between  $\bar{P}_{XWR}$  and  $\bar{P}_{CML}$  is shown for all observations in the pre- and post-  
 513 plateau periods (in total 85 data points) in Fig. 11a.  $\bar{P}_{CML}$  was generally lower, and especially  
 514 when  $\bar{P}_{XWR} < 20$  mm/h, then  $\bar{P}_{CML}$  was consistently very low. This suggests that XWR is more  
 515 sensitive to light rain than CML, as was observed when comparing with the municipal gauge  
 516 (Section 5.2.3). Hypothesizing that the difference between  $\bar{P}_{XWR}$  and  $\bar{P}_{CML}$  was related to the  
 517 XWR variability over the link, Fig. 11b shows the difference as a function of the X-band  
 518 standard deviation  $\sigma_{XWR}$ . Despite a substantial scatter, a reasonably linear trend is suggested  
 519 ( $R^2=0.31$ ) with  $\bar{P}_{CML}$  gradually underestimating more as the standard deviation increases.



520 **Figure 11.** a) Mean rainfall intensity  $P$  (mm/h) along the CML link as estimated by CML and XWR  
 521 observations for 85 timesteps, before and after the plateau. b) Difference between CML and XWR  
 522 mean intensity values as a function of XWR standard deviation  $\sigma_{XWR}$  along the CML link.  
 523

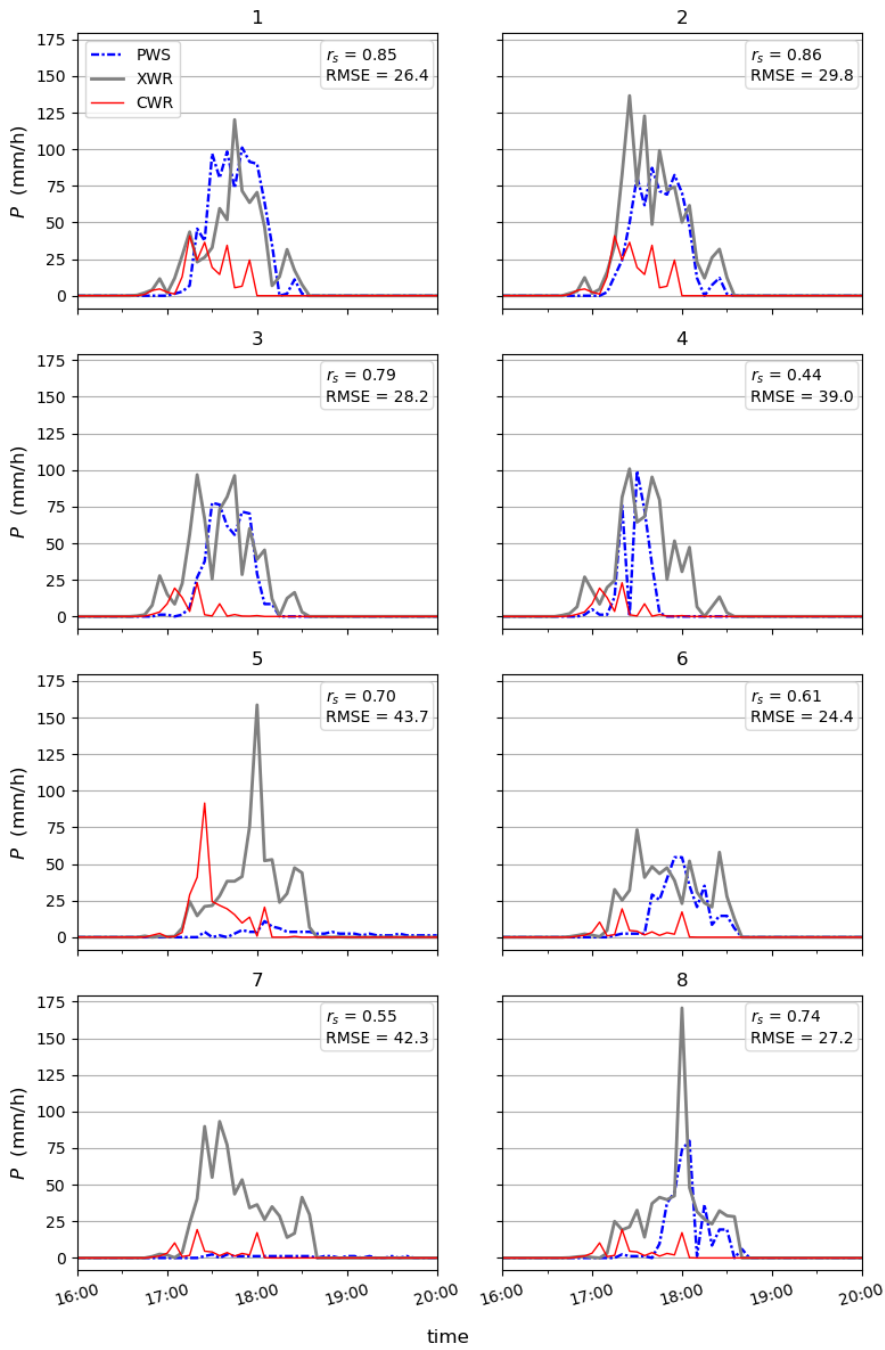
### 524 5.2.5 Personal Weather Stations

525 This section starts with the results of the PWS quality control, before presenting the event  
 526 observations. No faulty zeros or high influxes were detected during the event at any of the  
 527 eight PWS in the area of interest. Three of the PWS – PWS 1, PWS 3 and PWS 4 – were  
 528 flagged as station outliers. Nevertheless, all PWS were considered for further analysis to  
 529 compare the output of the PWS quality control with traditional evaluation metrics. The eight  
 530 PWS had between 25 and 29 stations within a 10 km radius that were included in the  
 531 neighboring checks.

532 The PWS time series were also checked for the full year 2022. PWS 1 and 4 were flagged as  
 533 faulty zeroes continuously during the winter months but had no Faulty Zero flags during the  
 534 summer months (see Appendix A3, Fig. A2). The other PWS got intermittently flagged, but  
 535 overall, there were few Faulty Zero flags during the year. No high influxes were detected at

536 any PWS during 2022. All stations were flagged as Station Outliers during extended periods  
537 throughout the year, except one (PWS 6), which only had a few Station Outlier flags in  
538 December 2022 (see Appendix A3, Fig. A3).

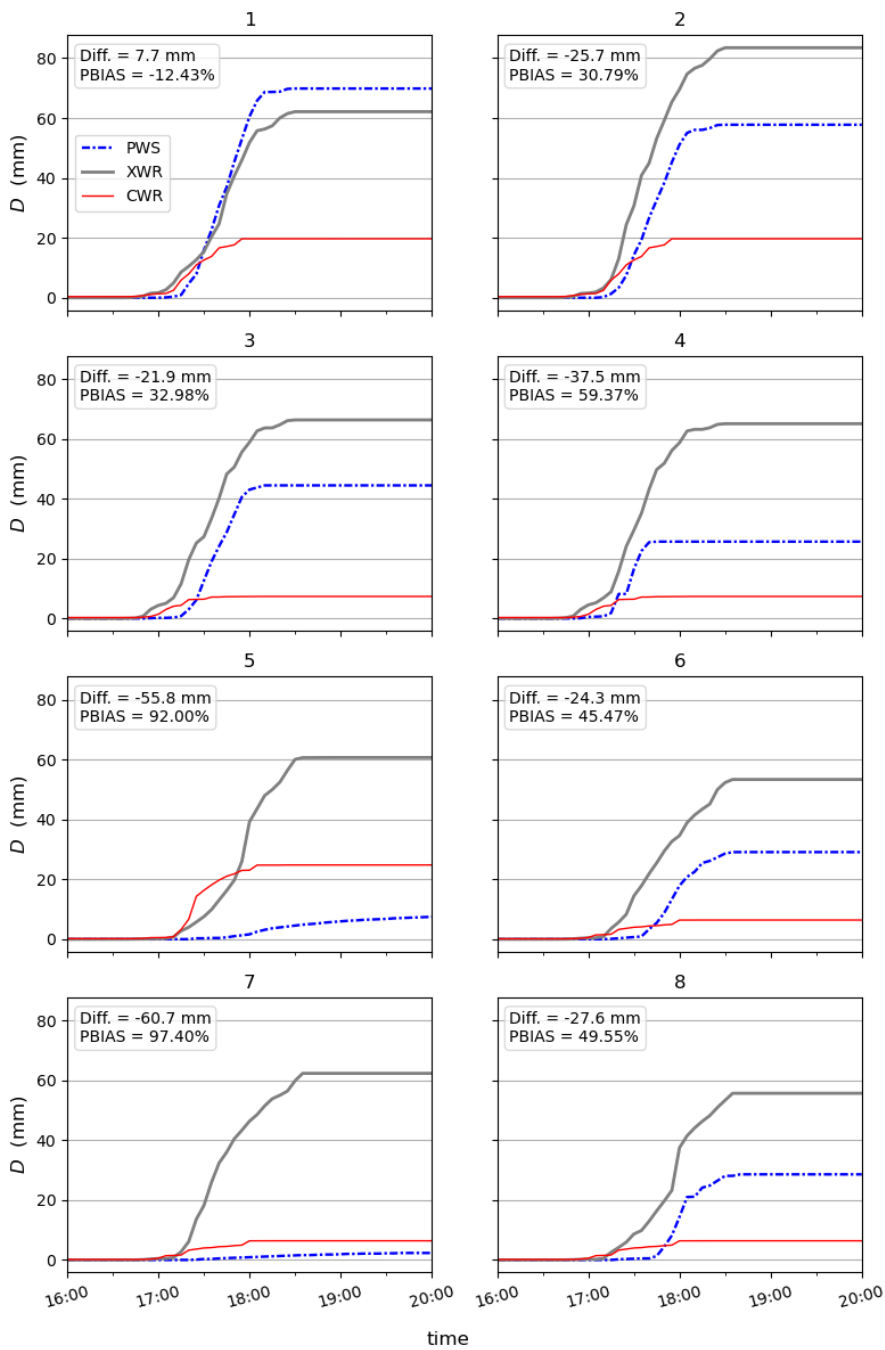
539 Figure 12 shows the rainfall intensity  $P$  (mm/h) observed by the eight PWS and XWR sampled  
540 at the PWS location, with metrics calculated with XWR as reference. The correlation with XWR  
541 was generally quite high, above 0.7 for five of the eight PWS. The CWR sampled at the PWS  
542 locations is included for comparison. Note that the CWR time series are identical for PWS 1  
543 and 2, PWS 3 and 4, and PWS 6, 7 and 8 respectively, meaning that the PWS are situated in  
544 the same CWR grid cell.



545  
 546 **Figure 12.** Rainfall intensity  $P$  (mm/h) for PWS 1-8. Spearman rank coefficient  $r_s$  (-) and RMSE (mm/h)

547 *calculated with XWR sampled at each PWS as reference. CWR sampled at each PWS included for*  
548 *comparison.*

549 Figure 13 shows the accumulated rainfall depth  $D$  (mm) for the event. Almost all PWS  
550 significantly underestimated the total depth compared with the XWR reference. However, the  
551 estimate was closer to the reference compared with CWR, with two exceptions (PWS 5 and  
552 PWS 7). PWS 1 is the only PWS that overestimated compared with the reference, in total 7.7  
553 mm (PBIAS -12.43%).



554  
 555 **Figure 13.** Accumulated depth  $D$  (mm), difference in total depth and PBIAS calculated for PWS 1-8 with

556 *XWR sampled at each PWS as reference. CWR sampled at each PWS included for comparison.*

## 557 5. Discussion

558 This study investigates the capacity of second- and third-party sensors to observe short-  
559 duration extreme rainfall, compared with a conventional rainfall monitoring network. Sweden's  
560 national rainfall monitoring network, composed of automatic and manual weather stations and  
561 a CWR composite, is used as a conventional network in the study. The second-party network  
562 consists of a municipal rain gauge and an XWR operated by a local water utility company. CML  
563 and PWS are studied as third-party sensors. First, a long-term analysis of the municipal gauge  
564 is performed by cross-referencing two years of data with the national monitoring network. In  
565 this way, the municipal gauge is established as a trusted reference sensor for the study. Then,  
566 a convective rainfall event that hit southwestern Sweden in the late afternoon of 18 August  
567 2022 is selected as a case study. The event analysis focuses on the urban area of Båstad, a  
568 small seaside municipality on the coast of Laholm Bay, as this location was particularly affected  
569 according to media reports.

570 No weather station in the national monitoring network captured the magnitude of the event as  
571 reported by the media (Section 5.2.2). The rainfall observed by the automatic and manual  
572 weather stations during the day of the event corresponded to a return period of less than one  
573 year, which suggests that the rainfall fell between the stations. CWR recorded a maximum total  
574 depth of 65 mm corresponding to a return period of 400 years, but the observation was made  
575 south of the Båstad urban area (Fig. 5). Within the area of interest, the maximum recorded  
576 depth was only 25 mm, which does not align with the municipal observations and the media  
577 reports about flooded streets and buildings.

578 CWR peaked at 92 mm/h at 17:25 in the sampling point at PWS 5, which is the only CWR  
579 observation in the expected magnitude of the event based on the municipal gauge. The specific  
580 CWR used in the study (location *Ångelholm*) is known to be affected by partial beam blockage  
581 which likely caused the severe underestimation (Appendix A1). This suggests that the siting of  
582 the radar should be improved, for example by vegetation clearance, increasing the height of  
583 the radar tower or relocation, to allow for better rainfall estimates. The underestimation may  
584 also be attributed to, for example, a lack of dual-polarization variables, insufficient attenuation  
585 correction (Hosseini et al., 2020), radar calibration or ground clutter removal (van de Beek et  
586 al., 2016). Furthermore, the use of the traditional *Z-R* (reflectivity – rain rate) relationship based  
587 on Marshall-Palmer coefficients (Marshall and Palmer, 1948) (Marshall and Palmer, 1948b) in  
588 the CWR data processing may not be well suited for convective storms. SMHI is currently  
589 developing new *Z-R* relationships for different weather conditions to improve the accuracy of  
590 CWR-based precipitation estimates in the future.

Formatted: English (United States)

Formatted: English (United States)

Formatted: English (United States)

591 When turning to the second-party data, the magnitude of the event is starting to emerge. The  
592 municipal gauge showed good agreement with the national monitoring network in the long-  
593 term analysis and observed a ~700-year rainfall in the Båstad urban area during the event  
594 (Section 5.2.3). The XWR sampled at the location of the municipal gauge recorded a total  
595 depth of 78.4 mm, corresponding to a return period of ~800 years. It must be emphasized that  
596 estimated long return periods are highly dependent on the estimated rainfall duration, which  
597 may vary significantly in space and are difficult to firmly determine (Section 5.2.1).  
598 Furthermore, return period estimates are highly uncertain and should therefore not be  
599 quantified with high precision. In this context, a difference of ~100 years must be considered  
600 relatively small and rather indicates a good agreement between the estimates.

601 XWR could accurately estimate the total rainfall depth compared with the municipal gauge  
602 (PBIAS 9.4%). However, both radars showed a relatively low correlation with the reference;  
603 0.56 for XWR (Fig. 8) and 0.4 for CWR (Fig. 6). The low correlation may be due to differences  
604 in the observation height between radar and gauge measurements. This could partly be  
605 accounted for by applying time lags and shifting the time series 5 and 10 minutes respectively,  
606 but also highlights the importance of accurate time stamping in the context of convective rainfall  
607 measurements.

608 XWR observations, particularly at long ranges, are known to be affected by signal attenuation  
609 due to interactions with hydrometeors (Bobotová et al., 2022; Lengfeld et al., 2016). However,  
610 XWR performed well during this event at a 40-km range, likely because the event occurred  
611 locally under a mostly clear sky. Remarkably, there was no intervening precipitation between  
612 the radar and the target area. Furthermore, it is perceived that beam overshooting was unlikely  
613 due to the higher altitude of summer precipitation compared to the XWR sampling volume at  
614 the lowest elevation angle.

615 One CML with a length of 4.8 km is located in the area of interest. The CML observed a  
616 similar duration of the event as the XWR reference (Section 5.2.4). The correlation was  
617 spuriously high (0.9) due to lack of variation in the CML rainfall rate, as it reached a 'plateau'  
618 and stayed constant at this level for about 30 minutes, leading to an underestimation of the  
619 total depth. This effect is sometimes referred to as 'blackout' (Polz et al., 2023) and appears  
620 when the radio signal is completely attenuated by heavy rainfall (ITU-R, 2005). Telecom  
621 network providers design the CML hardware so that transmission outages are allowed to  
622 occur 0.01% of the time on an annual basis. Indeed, Polz et al. (2023) found that blackout  
623 gaps were present in less than 1% of attenuation data from 4000 CMLs over 3 years in  
624 Germany, and that the effect on long-term timescales was generally low. However, the  
625 probability of a blackout at rainfall intensities above 100 mm/h was above 40%, which implies  
626 that the CML technology currently has limitations in quantifying extreme events.

Formatted: English (United States)

Formatted: English (United States)

Formatted: English (United States)

627 The analysis of XWR data along the CML link revealed some notable results. Firstly, the XWR  
628 data at some time steps exhibited a large bin-to-bin variability, sometimes shifting from one  
629 intensity level to another (Fig.10b). This can be attributed to the turbulent nature of convective  
630 storms, and local attenuations of XWR signals during heavy rain bursts due to possible  
631 uncertainties in the attenuation correction. Despite overall agreement between  $\hat{P}_{XWR}$  and  $\hat{P}_{CML}$   
632 along the link, a substantial scatter was found where, in particular, low intensities were  
633 consistently higher in the XWR data than CML (Fig. 11). Generally, there was a clear indication  
634 that the CML underestimation increased with increasing rainfall intensity as well as variability  
635 along the link. Berne & Uijlenhoet (2007) and de Vos et al., (2018) showed that spatial  
636 variability of rainfall can significantly affect CML-based rainfall estimates. A systematic  
637 underestimation of CML is expected for  $\alpha < 1$  (see Appendix A2, Eq. A2) (Leijnse et al., 2010).  
638 Notably, the estimations of the event duration based on radars and CML were significantly  
639 different from the in-situ gauge observations. For example, the municipal gauge started to  
640 observe the event 20 minutes after CWR. These discrepancies could be attributed to the larger  
641 sensitivity of CML and radars to light rainfall and slow accumulations in the tipping-bucket  
642 gauge during light drizzles preceding the heavy bursts.

643 Regarding the eight PWS in the area of interest, the tipping bucket mechanism seems to have  
644 reached a maximum tipping frequency (i.e., detectable intensity) during the highest-intensity  
645 periods, as no observation exceeded 100 mm/h (Fig. 12). A similar tendency has been  
646 observed by others (Lussana et al., 2023; Wolf and Larsson, 2024). Among the PWS with  
647 lowest RMSE, this led to a PBIAS of 30-40% compared with the XWR reference (Fig. 13).  
648 PWS 1 performed reasonably well on all evaluation metrics with a Spearman correlation of  
649 0.85, RMSE 26.4 mm/h and PBIAS -12.4%. In most cases, the correlation with reference was  
650 medium to high, with only two PWS (PWS 4 and 7, Fig. 12) having a correlation below 0.6.

651 We applied a quality control specifically designed for PWS rainfall data, *pypwsqc* (Chwala et  
652 al., n.d.) on the event and full year 2022 (Section 5.2.5). The algorithm applies three filters –  
653 Faulty Zeroes filter, High Influx filter, and Station Outlier filter – to assess the quality of each  
654 time step by utilizing neighbor checks with nearby stations. No faulty zeroes were detected  
655 during the event, which is reasonable as all PWS in the area of interest measured rainfall at  
656 all timesteps. No high influxes were found, suggesting that all PWS in the area measured  
657 enough rainfall not to trigger high influx flags at the neighboring stations. On the other hand,  
658 no high influx was detected at any PWS during the entire year 2022. There might indeed not  
659 have been any high influx recorded by any of the 58 PWS on the Bjäre Peninsula in 2022, but  
660 the results also raise the question of whether the filter parameters should be tuned differently  
661 to better capture unrealistically high inflows.

Formatted: Swedish (Sweden)

Formatted: Swedish (Sweden)

Formatted: Swedish (Sweden)

Field Code Changed

Field Code Changed

Formatted: English (United States)

Formatted: English (United States)

Formatted: English (United States)

662 Regarding the Station Outlier filter, three stations were flagged as station outliers during the  
663 event – PWS 1, PWS 3 and PWS 4. However, when inspecting the time series and evaluation  
664 metrics for these stations, it appeared that PWS 1 and PWS 3 had among the highest  
665 correlations and lowest RMSE of all PWS and generally showed a reasonable rainfall pattern  
666 compared with the other PWS (Fig. 12). These results point to a limitation of neighboring  
667 checks in the context of convective storms. PWS 1, PWS 3 and PWS 4 are all located in the  
668 western part of Båstad. As such, the Station Outlier filter considered the observations of PWS  
669 located further to the west on the Bjäre Peninsula, which experienced a total depth of only 10  
670 mm according to the XWR observations. The high spatial variability of the event therefore  
671 triggered station outlier flags at the three PWS located closest to the drier area, even if two of  
672 them performed well when compared with the XWR reference.

673 The parameter settings suggested in literature (Section 4.4) (de Vos et al., 2019) were changed  
674 in the Station Outlier filter. However, it is not expected that the changes created these results  
675 as the filter would not have been possible to apply at all for the event with the original numbers  
676 as there were too few wet time steps in the weeks preceding the storm. If the flagged PWS  
677 had been removed from further analysis based on the results from the Station Outlier filter,  
678 sound observations would have been lost. Conversely, the performance of PWS 5 and PWS  
679 7 was very poor compared with the XWR reference, but these stations were not flagged in the  
680 automatic quality control. Future research should explore how the spatial density of PWS and  
681 the considered evaluation range influence the capability of neighbor checks to be applicable  
682 as quality control protocols for localized rainfall.

683 The findings of this study align with the well-established fact that conventional monitoring  
684 networks have limitations in terms of observing convective rainfall. To strengthen capacity in  
685 this field, NMHS can include second-party data in operational tools and workflows. However,  
686 differences in acquisition protocols, data formats etc. adopted by different actors may cause  
687 an additional burden and hinder the integration of second-party sensors. Importantly, Skåne  
688 County has an excellent coverage of second-party sensors thanks to the combination of XWR  
689 and rain gauges operated by local authorities, which is certainly not the case for all points of  
690 interest, particularly in countries with limited resources (Winsemius et al., 2018). In those  
691 cases, NMHS can turn to third-party sensors, particularly CML that are typically available in  
692 populated settlements across the globe (Chwala and Kunstmann, 2019; Blettner et al., 2023).  
693 However, the results of this study suggest that these sensors currently have limitations in  
694 quantifying the correct magnitude of convective storms. Still, the results show that third-party  
695 data may assist in detecting storm durations and the spatial distribution of rainfall.

696 Regarding limitations of the study, a few remarks can be made. First, there are uncertainties  
697 associated with all observations in the study, especially the indirect rainfall measurements

Formatted: English (United States)

Formatted: English (United States)

Formatted: English (United States)

698 (radars and CML) and the PWS. The long-term assessment of the municipal gauge, combined  
699 with the good agreement between the municipal gauge and XWR, still provide solid evidence  
700 for the actual magnitude of the event. Secondly, some findings are expected to be specific for  
701 this study, such as the low performance by CWR caused by beam blockage in the area of  
702 interest. On the other hand, the underestimation of rainfall observed by the third-party network  
703 aligns with previous studies. It is also expected that quality control protocols that utilize  
704 neighboring checks will be problematic for other convective storms, depending on the station  
705 network density and considered range of the analysis. Although no general conclusions can  
706 be drawn from a case study, we believe that the depth of this analysis contributes to the  
707 understanding of advantages and limitations when observing convective rainfall with second-  
708 and third-party sensors.

## 709 6. Conclusion

710 This study investigated the capacity of second- and third-party sensors to observe short-  
711 duration extreme rainfall compared with a conventional rainfall monitoring network in a case  
712 study. The results show that the conventional network underestimated the total rainfall depth  
713 of the event and was unable to fully capture the extreme spatial variability of the convective  
714 storm. Only when considering observations from second- and third-party sensors, more  
715 accurate representations of the magnitude and spatial extent of the storm could be obtained,  
716 which suggests that NMHS could utilize these sensors to improve observations of convective  
717 rainfall. However, second-party sensors are not always available, particularly in resource-  
718 strained settings. Furthermore, the results suggest that third-party sensors can assist in  
719 detecting storm durations and spatial variability of rainfall but have limitations in quantifying  
720 the correct magnitude of convective storms. Third-party data may also be difficult to obtain  
721 for NMHS and has known problems with data quality. Future research is suggested to  
722 continue the efforts on quality control of third-party data, especially related to extreme  
723 events. In addition, more research is needed on the integration of second- and third-party  
724 data in the workflows of NMHS.

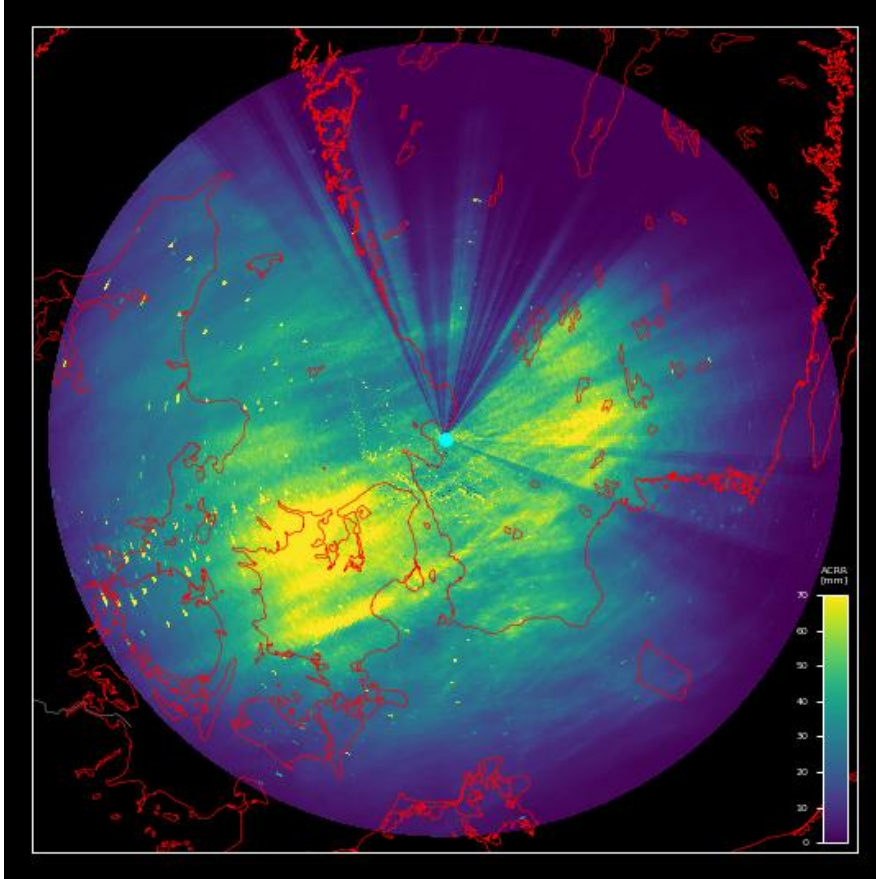
## 725 Appendix A

### 726 A.1 Vegetation affecting the Ängelholm radar location

727 The *Ängelholm* radar location is affected by partial beam blockage in a circular sector of  
728 around 60 degrees to the North (Fig. A1) (SMHI, 2025a). Båstad is located 6 km to the north  
729 of the radar. The figure shows accumulated precipitation detected by the radar during the  
730 period 3-17 October, 2019. Darker color indicates less total precipitation.

Formatted: Swedish (Sweden)

Formatted: Swedish (Sweden)



731

732 **Figure A1.** Accumulated precipitation detected by CWR Ängelholm, 3-17 October, 2019.

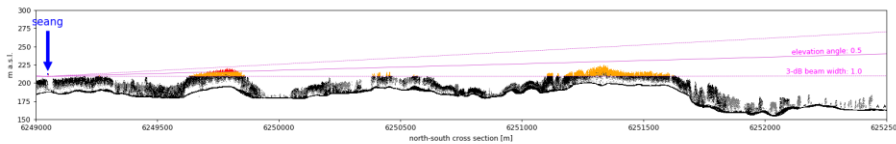
733 The partial beam blockage is caused by vegetation within 1 km north of the radar location.

734 Fig. A2 shows the Ängelholm radar beam in the north direction overlaid with a point cloud of

735 vegetation based on aerial laser scans (Lantmäteriet, 2025). Note that the figure reflects the

736 status as of 2019 and the vegetation has likely grown taller since.

Formatted: English (United States)



737

738 **Figure A2.** Ängelholm radar beam in the north direction overlaid with a point cloud of vegetation  
739 based on aerial laser scans (Lantmäteriet, 2025).

Formatted: English (United States)

## 740 A.2 CML processing

741 When estimating rainfall intensity from CML data, the first step is to identify a link-specific  
742 threshold for classification of wet and dry timesteps. The challenge is to detect small rainfall  
743 volumes (true wet periods) without including too many dry periods with strong attenuation  
744 from other causes, such as changes in water vapor content or air temperature (false wet  
745 periods). Several approaches have been suggested in literature (Rayitsfeld et al., 2012;  
746 Wang et al., 2012; Cherkassky et al., 2014; Overeem et al., 2016). Schleiss & Berne (2010)  
747 proposed a simple classification method that considers the rolling standard deviation of the  
748 attenuation, assuming that the variability is small during dry periods and large during wet  
749 periods. The time step is classified as dry if the variability falls below a defined threshold  
750 value, which must be calibrated with secondary observations nearby the link. More recently,  
751 machine learning approaches has shown strong potential to effectively classify wet and dry  
752 timesteps in CML data (Habi and Messer, 2018; Polz et al., 2020; Øydvin et al., 2024).

Formatted: English (United States)

Formatted: English (United States)

753 The second step is to define a 'baseline level', that is, RSL during dry weather. This is used as  
754 the reference level for the rain attenuation calculation and is typically based on the signal  
755 attenuation during dry time steps preceding a wet period (Andersson et al., 2022). In addition,  
756 the signal is often corrected for additional attenuation caused by water on the cover of the  
757 antenna, so-called 'wet antenna attenuation' (e.g., Leijnse et al., 2007a, 2008; Graf et al.,  
758 2020). Finally, the corrected attenuation is converted into rain rate using an inverted power law  
759 relationship. The MEMO method was developed and tested on an open data set ('OpenMRG')  
760 that consists of 364 CML and 11 rainfall gauges in Gothenburg, Sweden, for the period June-  
761 August 2015 (Andersson et al., 2022). The processing steps of the MEMO methodology are  
762 outlined below.

Formatted: English (United States)

Formatted: English (United States)

### 763 A.2.1 Data pre-processing

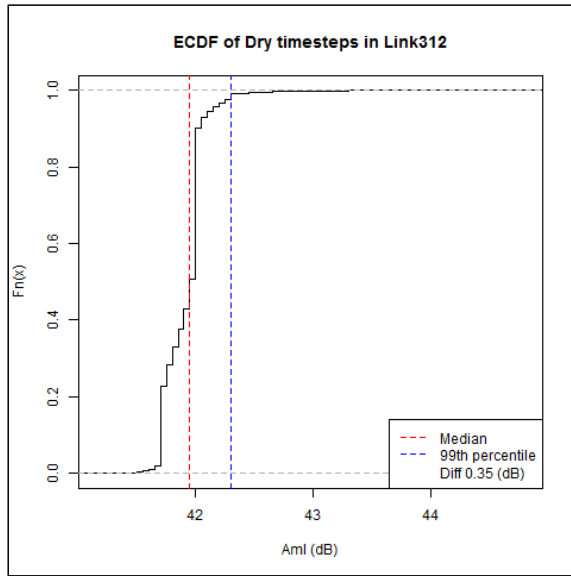
764 The 10-second attenuation was calculated by taking the difference between TSL and RSL.  
765 Then, the median value over a 1-minute period  $A_m$  was taken for all minutes that had more  
766 than four 10-second values in one minute and if less data were available, that minute was  
767 flagged as missing data.

### 768 A.2.2 Wet-dry classification

769 Sub-links in the *OpenMRG* dataset were scrutinized to find a wet-dry classification method that  
770 does not rely on secondary observations. The links considered were located within 500 m from  
771 a municipal rain gauge in Gothenburg that records at 1-minute temporal resolution, resulting  
772 in 72 links. First, dry time steps recorded by the station between 2015-05-14 to 2015-08-31  
773 were considered. A time buffer of 30 minutes was added before and after each rain event  
774 recorded by the rain gauge, to consider that rainfall arrives at different timesteps to the links.  
775 The 99<sup>th</sup> percentile of  $A_m$  at dry timesteps identified by the rain gauge was considered to

Formatted: English (United States)

776 address that the links may record rainfall that was missed by the rain gauge. Then, the  
777 empirical distribution of  $A_{mi}$  at the dry timesteps was plotted and inspected for the 72 links. An  
778 example is shown in Fig. A3. In this example, the difference between the median and 99<sup>th</sup>  
779 percentile of the attenuation is 0.35 dB.



780

781 **Figure A3.** Example of empirical distribution of attenuation level ( $A_{mi}$ ) at dry timesteps for Link 312.

782 The plots showed that the difference in  $A_{mi}$  between the median attenuation and the 99<sup>th</sup>  
783 percentile was typically between 0.35-0.6 dB at dry timesteps. However, the difference for one  
784 link with considerable fluctuations in signal attenuation was 1.7 dB. Based on these results, it  
785 was decided to set the threshold for the wet-dry classification to the median attenuation over  
786 the past 2 weeks plus an additional 1.7 dB (here called the '*median buffer method*'). In this  
787 study, where only two days of data was available, the median was taken over all available  
788 preceding time steps.

789 The median buffer method was compared with classifying all timesteps with attenuation above  
790 the median of the last two weeks as wet ('*median method*') and the method presented by  
791 Schleiss and Berne (2010) ('*Schleiss method*'). The median method resulted in overestimation  
792 of the number of wet timesteps compared with the rain gauge. The Schleiss method performed  
793 similarly to the median buffer method in correctly identifying the number of wet timesteps but  
794 resulted in some outliers and produced more false wet time steps. Based on these results, the  
795 median buffer method was used for further analysis.

### 796 A.2.3 Baseline definition

797 The baseline  $A_{bl}$  is the expected difference between TSL and RSL during dry weather. This  
798 means that during dry periods, based on the wet-dry classification in the previous step, the  
799 baseline is equal to the attenuation  $A_{ml}$ . During wet periods, the baseline is taken as the  
800 median of the last  $N$  timesteps from the first wet timestep. A suitable reference period for  $N$   
801 was found to be 240 minutes.

### 802 A.2.4 Conversion of net attenuation to rain rate

803 By subtracting the baseline from the attenuation, the net attenuation  $A_{nl}$  was found as

$$A_{nl} = A_{ml} - A_{bl} \quad (A1)$$

804 Following common practice in CML literature (Leijnse et al., 2007b; Messer et al., 2006),  
805 specific attenuation ( $dB km^{-1}$ ) was converted to rain rate ( $P_{raw}$ ) using link length ( $L$ , km) and the  
806 power-law relationship:

$$\frac{A_{nl}}{L} = k P_{raw}^{\alpha} \quad (A2)$$

807 The parameters  $k$  and  $\alpha$  depend on link frequency, the polarization state, and the elevation  
808 angle of the signal path and was found by applying the equations derived by ITU-R (2005). For  
809 the link in this paper,  $k = 0.13$  and  $\alpha = 0.96$  (23.1 GHz, vertical polarization). In contrast to  
810 radar scatter, the sensitivity to DSD (Eq.1) is very limited around 30 GHz because  $\alpha$  is  
811 approximately 1 in this range, suggesting a nearly linear relation between net attenuation and  
812 rain rate (Chwala and Kunstmann, 2019). At frequencies further from 30 GHz, DSD will play a  
813 larger role and biases can occur. Most links in Sweden operate near 30 GHz (Andersson et  
814 al., 2022).

### 815 A.2.5 Bias correction based on link length

816 The derived rain rate was analyzed for the 72 links situated within 500 m range from the 11  
817 rain gauges in the *OpenMRG* dataset for July 2015. When plotting the residuals of the rain rate  
818 at the closest gauge against 15-min accumulated net attenuation of the link, a linear  
819 relationship was found, indicating potential for bias correction. The slope of the residuals was  
820 derived by linear regression for each link and plotted against the link frequency, link length and  
821 the parameters  $k$  and  $\alpha$  in Eq. A2. The most distinct relationship was found for link length,  
822 suggesting that the shorter the length, the higher the slope of the residuals. One probable  
823 reason for the relationship is the wet-antenna effect, which is stronger over shorter distances  
824 (Chwala and Kunstmann, 2019).

825 It was found that the slope of the regression line of the residuals could be estimated from link  
826 length by applying a simple inverse equation:

Formatted: English (United States)

Formatted: English (United States)

Formatted: English (United States)

Formatted: English (United States)

Formatted: English (United States)

$$Slope = f \times \frac{1}{L^g} + h \quad (A3)$$

827 where  $L$  is the link length. The parameters  $f$ ,  $g$ , and  $h$  were optimized by minimizing the Mean  
828 Absolute Error for the 72 links, arriving at 2.85214, 1.672 and 0.1615, respectively. The bias  
829 corrected rain rate for the CML in Båstad was then found by calculating the correction factor:

$$CF_A = 2.85214 * (1/L^{1.672}) + 0.1615 \quad (A4)$$

830

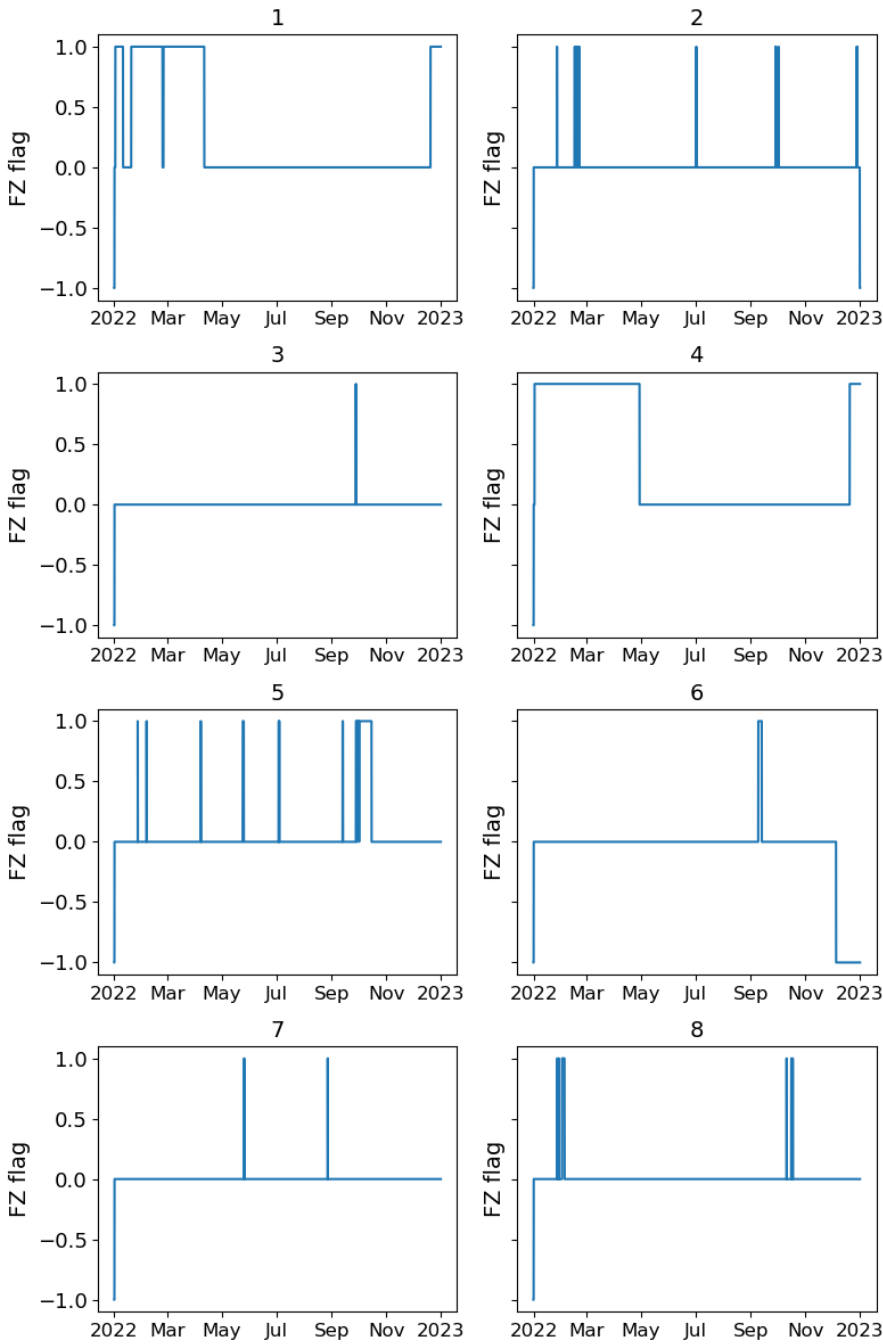
831 where  $L$  is 4.8 km in this case. Then, applying the factor to the derived rain rate:

$$P_{CML} = P_{raw} - (A_{nl} * CF_A) \quad (A5)$$

832

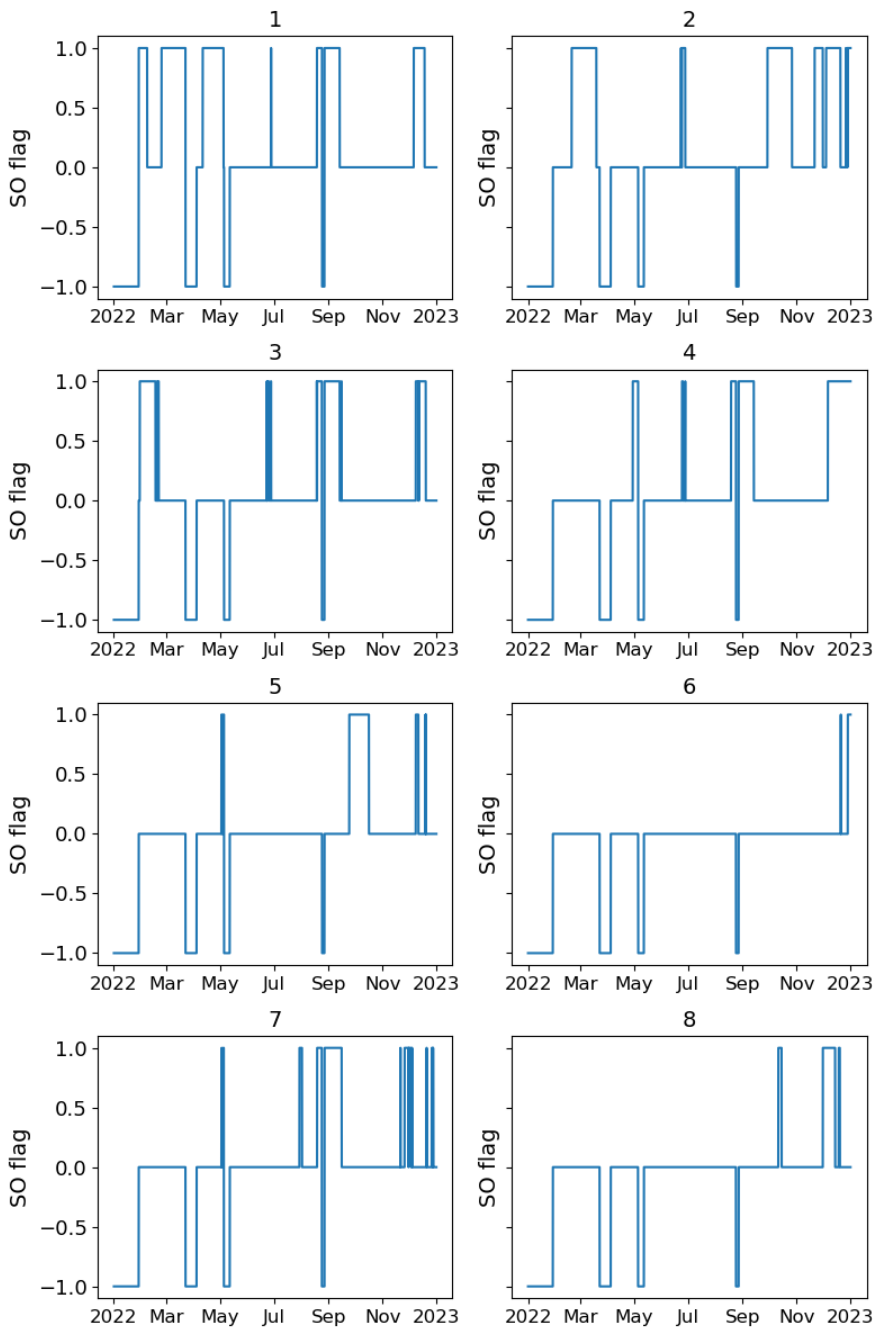
### 833 [A.3 PWS quality control 2022](#)

834 Figure A4 shows Faulty Zero (FZ) flags for the eight PWS in the area of interest for the full  
835 year 2022.



836  
 837 **Figure A4.** Faulty Zero (FZ) flags 2022. 1 = FZ flag, 0 = no FZ-flag, -1 = FZ-filter could not be applied.

838 Figure A5 shows Station Outlier (SO) flags for the eight PWS in the area of interest for the  
839 full year 2022.



840

841 **Figure A5.** SO-flags 2022. 1 = SO flag, 0 = no SO-flag, -1 = SO-filter could not be applied.

## 842 Data availability

843 National weather station data and C-band radar composite are available from SMHI's open  
844 data archive ([www.smhi.se/data](http://www.smhi.se/data)). The processed national data are available on request.

845 Data from the municipal gauge and X-band radar is the property of Nordvästra Skånes  
846 Vatten och Avlopp, NSVA. CML data is the property of the telecom companies Ericsson AB  
847 and Tre. PWS data is the property of Netatmo. However, Netatmo data can be openly  
848 accessed through their API: <https://weathermap.netatmo.com>

Field Code Changed

Field Code Changed

## 849 Author contribution

850 LPW processed gauge data. LPW and RvdB processed CWR data. HaH, LPW and RvdB  
851 processed XWR data. RvdB and LPW processed CML data. JA developed the CML processing  
852 methodology. LPW implemented the PWS quality control. LPW, JO and HaH performed data  
853 analysis. All authors were involved in the writing and editing of this manuscript.

## 854 Competing Interests

855 The authors declare that they have no conflict of interest.

## 856 Acknowledgements

857 The authors would like to thank NSVA for sharing tipping bucket data and Ericsson AB and  
858 Tre for sharing CML data. Lennart Simonsson processed PWS data to NetCDF-files. Riejanne  
859 Mook improved the CML processing code. Daniel Johnson provided information on the partial  
860 beam blockage of the *Ängelholm* C-band radar. The development of *pypwsqc* was carried out  
861 jointly with Christian Chwala within the working group 2 of the COST Action OpenSense  
862 CA20136.

## 863 Financial support

864 The paper was supported by the projects SPARC (*Stakeholder participation for climate  
865 adaptation – data crowdsourcing for improved urban flood risk management*, grant 2021-  
866 02380 Formas) and HyPrecip (*Hyper-resolution multi-dimensional precipitation information  
867 for analysis and modelling: urban and rural applications*, grant 2021-01629 Formas). The  
868 development of *pypwsqc* received funding from the European Union's Framework  
869 Programme for Research & Innovation as part of the COST Action *OpenSense* [CA20136],  
870 as supported by the COST Association (European Cooperation in Science and Technology).

## 871 References

- 872 Andersson, J. C. M., Olsson, J., van de Beek, R. (C. Z.), and Hansryd, J.: OpenMRG: Open data from  
873 Microwave links, Radar, and Gauges for rainfall quantification in Gothenburg, Sweden, *Earth Syst. Sci.*  
874 *Data*, 14, 5411–5426, <https://doi.org/10.5194/essd-14-5411-2022>, 2022.
- 875 Bárdossy, A., Seidel, J., and El Hachem, A.: The use of personal weather station observations to  
876 improve precipitation estimation and interpolation, *Hydrol. Earth Syst. Sci.*, 25, 583–601,  
877 <https://doi.org/10.5194/hess-25-583-2021>, 2021.
- 878 Båserud, L., Lussana, C., Nipen, T. N., Seierstad, I. A., Oram, L., and Aspelien, T.: TITAN automatic  
879 spatial quality control of meteorological in-situ observations, in: *Advances in Science and Research,*  
880 *19th EMS Annual Meeting: European Conference for Applied Meteorology and Climatology 2019 -*,  
881 153–163, <https://doi.org/10.5194/asr-17-153-2020>, 2020.
- 882 Battan, L. J.: *Radar Observation of the Atmosphere*, Rev. ed., University of Chicago Press, 1973.
- 883 van de Beek, C. Z., Leijnse, H., Hazenberg, P., and Uijlenhoet, R.: Close-range radar rainfall estimation  
884 and error analysis, *Atmospheric Meas. Tech.*, 9, 3837–3850, [https://doi.org/10.5194/amt-9-3837-](https://doi.org/10.5194/amt-9-3837-2016)  
885 2016, 2016.
- 886 Bengtsson, L.: Regn i Båstad, *Vatten Tidkr. För Vattenvård J. Water Manag. Res.*, (1-2), 61–70, 2023.
- 887 Berne, A. and Uijlenhoet, R.: Path-averaged rainfall estimation using microwave links: Uncertainty  
888 due to spatial rainfall variability, *Geophys. Res. Lett.*, 34, <https://doi.org/10.1029/2007GL029409>,  
889 2007.
- 890 Blettner, N., Fencel, M., Bareš, V., Kunstmann, H., and Chwala, C.: Transboundary rainfall estimation  
891 using commercial microwave links, *Earth Space Sci.*, 10, e2023EA002869,  
892 <https://doi.org/10.1029/2023EA002869>, 2023.
- 893 Bobotová, G., Sokol, Z., Popová, J., Fišer, O., and Zacharov, P.: Analysis of two convective storms  
894 using polarimetric X-band radar and satellite data, *Remote Sens.*, 14, 2294,  
895 <https://doi.org/10.3390/rs14102294>, 2022.
- 896 Boonstra, M. M. T.: *Delft Measures Rain. A quality assessment of precipitation measurements from*  
897 *personal weather stations*, Master Thesis, Delft University of Technology, the Netherlands, 2024.
- 898 Cherkassky, D., Ostrometzky, J., and Messer, H.: Precipitation classification using measurements from  
899 commercial microwave links, *IEEE Trans. Geosci. REMOTE Sens.*, 52, 2350–2356,  
900 <https://doi.org/10.1109/TGRS.2013.2259832>, 2014.
- 901 Chwala, C. and Kunstmann, H.: Commercial microwave link networks for rainfall observation:  
902 Assessment of the current status and future challenges, *WIREs Water*, 6, e1337,  
903 <https://doi.org/10.1002/wat2.1337>, 2019.
- 904 Chwala, C., Seidel, J., and Petersson Wårdh, L.: *OpenSenseAction/pypwsqc*, n.d.
- 905 Einfalt, T., Arnbjerg-Nielsen, K., Golz, C., Jensen, N.-E., Quirnbach, M., Vaes, G., and Vieux, B.:  
906 Towards a roadmap for use of radar rainfall data in urban drainage, *J. Hydrol.*, 299, 186–202,  
907 <https://doi.org/10.1016/j.jhydrol.2004.08.004>, 2004.

Formatted: English (United States)

Formatted: English (United States)

908 Fencel, M., Nebuloni, R., C. M. Andersson, J., Bares, V., Blettner, N., Cazzaniga, G., Chwala, C., Colli, M.,  
909 de Vos, L., El Hachem, A., Galdies, C., Giannetti, F., Graf, M., Jacoby, D., Victor Habi, H., Musil, P.,  
910 Ostrometzky, J., Roversi, G., Sapienza, F., Seidel, J., Spackova, A., van de Beek, R., Walraven, B.,  
911 Wilgan, K., and Zheng, X.: Data formats and standards for opportunistic rainfall sensors, *Open Res.*  
912 *Eur.*, 3, 169, <https://doi.org/10.12688/openreseurope.16068.2>, 2024.

913 Fuentes-Andino, D., Beven, K., Halldin, S., Xu, C.-Y., Reynolds, J. E., and Di Baldassarre, G.:  
914 Reproducing an extreme flood with uncertain post-event information, *Hydrol. Earth Syst. Sci.*, 21,  
915 3597–3618, <https://doi.org/10.5194/hess-21-3597-2017>, 2017.

916 Garcia-Marti, I., Overeem, A., Noteboom, J. W., de Vos, L., de Haij, M., and Whan, K.: From proof-of-  
917 concept to proof-of-value: Approaching third-party data to operational workflows of national  
918 meteorological services, *Int. J. Climatol.*, 43, 275–292, <https://doi.org/10.1002/joc.7757>, 2023.

919 Graf, M., Chwala, C., Polz, J., and Kunstmann, H.: Rainfall estimation from a German-wide commercial  
920 microwave link network: optimized processing and validation for 1 year of data, *Hydrol. Earth Syst.*  
921 *Sci.*, 24, 2931–2950, <https://doi.org/10.5194/hess-24-2931-2020>, 2020.

922 Graf, M., Chwala, C., Petersson Wårdh, L., and Seidel, J.: OpenSenseAction/pypwsqc: v0.2.1, ,  
923 <https://doi.org/10.5281/zenodo.16748098>, 2025.

924 Gravlund: [https://www.svt.se/nyheter/lokalt/helsingborg/kraftiga-skyfall-over-bastad-har-aldrig-](https://www.svt.se/nyheter/lokalt/helsingborg/kraftiga-skyfall-over-bastad-har-aldrig-varit-med-om-nagot-liknande)  
925 [varit-med-om-nagot-liknande](https://www.svt.se/nyheter/lokalt/helsingborg/kraftiga-skyfall-over-bastad-har-aldrig-varit-med-om-nagot-liknande), last access: 14 April 2025.

926 Guo, Y.: Updating Rainfall IDF Relationships to Maintain Urban Drainage Design Standards, *J. Hydrol.*  
927 *Eng.*, 11, 506–509, [https://doi.org/10.1061/\(ASCE\)1084-0699\(2006\)11:5\(506\)](https://doi.org/10.1061/(ASCE)1084-0699(2006)11:5(506)), 2006.

928 Gupta, H. V., Sorooshian, S., and Yapo, P. O.: Status of automatic calibration for hydrologic models:  
929 comparison with multilevel expert calibration, *J. Hydrol. Eng.*, 4, 135–143,  
930 [https://doi.org/10.1061/\(ASCE\)1084-0699\(1999\)4:2\(135\)](https://doi.org/10.1061/(ASCE)1084-0699(1999)4:2(135)), 1999.

931 Habi, H. V. and Messer, H.: Wet-dry classification using LSTM and commercial microwave links, in:  
932 2018 IEEE 10th Sensor Array and Multichannel Signal Processing Workshop (SAM), 2018 IEEE 10th  
933 Sensor Array and Multichannel Signal Processing Workshop (SAM), Sheffield, United Kingdom, 149–  
934 153, <https://doi.org/10.1109/SAM.2018.8448679>, 2018.

935 Hahn, C., Garcia-Marti, I., Sugier, J., Emsley, F., Beaulant, A.-L., Oram, L., Strandberg, E., Lindgren, E.,  
936 Sunter, M., and Ziska, F.: Observations from personal weather stations—EUMETNET interests and  
937 experience, *Climate*, 10, 192, <https://doi.org/10.3390/cli10120192>, 2022.

938 Hosseini, S. H., Hashemi, H., Berndtsson, R., South, N., Aspegren, H., Larsson, R., Olsson, J., Persson,  
939 A., and Olsson, L.: Evaluation of a new X-band weather radar for operational use in south Sweden,  
940 *Water Sci. Technol.*, 81, 1623–1635, <https://doi.org/10.2166/wst.2020.066>, 2020.

941 Hosseini, S. H., Hashemi, H., Larsson, R., and Berndtsson, R.: Merging dual-polarization X-band radar  
942 network intelligence for improved microscale observation of summer rainfall in south Sweden, *J.*  
943 *Hydrol.*, 617, 129090, <https://doi.org/10.1016/j.jhydrol.2023.129090>, 2023.

944 Hyndman, R. J. and Koehler, A. B.: Another look at measures of forecast accuracy, *Int. J. Forecast.*, 22,  
945 679–688, <https://doi.org/10.1016/j.ijforecast.2006.03.001>, 2006.

946 Imhoff, R. O., Brauer, C. C., Overeem, A., Weerts, A. H., and Uijlenhoet, R.: Spatial and temporal  
947 evaluation of radar rainfall nowcasting techniques on 1,533 events, *Water Resour. Res.*, 56,  
948 e2019WR026723, <https://doi.org/10.1029/2019WR026723>, 2020.

949 ITU-R: Recommendation ITU-R P.838-3: Specific attenuation model for rain for use in prediction  
950 methods., Radiocommunication Sector of International Telecommunication Union, 2005.

951 Kaiser, M., Günemann, S., and Disse, M.: Spatiotemporal analysis of heavy rain-induced flood  
952 occurrences in Germany using a novel event database approach, *J. Hydrol.*, 595, 125985,  
953 <https://doi.org/10.1016/j.jhydrol.2021.125985>, 2021.

954 Kumjian, M.: Principles and applications of dual-polarization weather radar. Part I: Description of the  
955 polarimetric radar variables, *J. Oper. Meteorol.*, 1, 226–242,  
956 <https://doi.org/10.15191/nwajom.2013.0119>, 2013.

957 Lantmäteriet: [https://www.lantmateriet.se/sv/geodata/vara-produkter/produktlista/laserdata-](https://www.lantmateriet.se/sv/geodata/vara-produkter/produktlista/laserdata-nedladdning-skog)  
958 [nedladdning-skog](https://www.lantmateriet.se/sv/geodata/vara-produkter/produktlista/laserdata-nedladdning-skog), last access: 7 November 2025.

959 Leijnse, H., Uijlenhoet, R., and Stricker, J. N. M.: Hydrometeorological application of a microwave link:  
960 2. Precipitation, *WATER Resour. Res.*, 43, W04417, <https://doi.org/10.1029/2006WR004989>, 2007a.

961 Leijnse, H., Uijlenhoet, R., and Stricker, J. N. M.: Rainfall measurement using radio links from cellular  
962 communication networks, *Water Resour. Res.*, 43, <https://doi.org/10.1029/2006WR005631>, 2007b.

963 Leijnse, H., Uijlenhoet, R., and Stricker, J. N. M.: Microwave link rainfall estimation: Effects of link  
964 length and frequency, temporal sampling, power resolution, and wet antenna attenuation, *Adv.*  
965 *Water Resour.*, 31, 1481–1493, <https://doi.org/10.1016/j.advwatres.2008.03.004>, 2008.

966 Leijnse, H., Uijlenhoet, R., and Berne, A.: Errors and uncertainties in microwave link rainfall  
967 estimation explored using drop size measurements and high-resolution radar data, *J.*  
968 *Hydrometeorol.*, 11, 1330–1344, <https://doi.org/10.1175/2010JHM1243.1>, 2010.

969 Lengfeld, K., Clemens, M., Merker, C., Münster, H., and Ament, F.: A simple method for attenuation  
970 correction in local X-band radar measurements using C-band radar data,  
971 <https://doi.org/10.1175/JTECH-D-15-0091.1>, 2016.

972 Lewis, E., Pritchard, D., Villalobos-Herrera, R., Blenkinsop, S., McClean, F., Guerreiro, S., Schneider, U.,  
973 Becker, A., Finger, P., Meyer-Christoffer, A., Rustemeier, E., and Fowler, H. J.: Quality control of a  
974 global hourly rainfall dataset, *Environ. Model. Softw.*, 144, 105169,  
975 <https://doi.org/10.1016/j.envsoft.2021.105169>, 2021.

976 Lussana, C., Baietti, E., Båserud, L., Nipen, T. N., and Seierstad, I. A.: Exploratory analysis of citizen  
977 observations of hourly precipitation over Scandinavia, *Adv. Sci. Res.*, 20, 35–48,  
978 <https://doi.org/10.5194/asr-20-35-2023>, 2023.

979 Mailhot, A. and Duchesne, S.: Design criteria of urban drainage infrastructures under climate change,  
980 *J. Water Resour. Plan. Manag.*, 136, 201–208, [https://doi.org/10.1061/\(ASCE\)WR.1943-](https://doi.org/10.1061/(ASCE)WR.1943-5452.0000023)  
981 [5452.0000023](https://doi.org/10.1061/(ASCE)WR.1943-5452.0000023), 2010.

982 Mandement, M. and Caumont, O.: Contribution of personal weather stations to the observation of  
983 deep-convection features near the ground, *Nat. Hazards Earth Syst. Sci.*, 20, 299–322,  
984 <https://doi.org/10.5194/nhess-20-299-2020>, 2020.

985 Marchi, L., Borga, M., Preciso, E., Sangati, M., Gaume, E., Bain, V., Delrieu, G., Bonnifait, L., and  
986 Pogačnik, N.: Comprehensive post-event survey of a flash flood in Western Slovenia: observation  
987 strategy and lessons learned, *Hydrol. Process.*, 23, 3761–3770, <https://doi.org/10.1002/hyp.7542>,  
988 2009.

989 Marshall, J. S. and Palmer, W. M. K.: The distribution of raindrops with size, *J. Atmospheric Sci.*, 5,  
990 165–166, [https://doi.org/10.1175/1520-0469\(1948\)005%253C0165:TDORWS%253E2.0.CO;2](https://doi.org/10.1175/1520-0469(1948)005%253C0165:TDORWS%253E2.0.CO;2), 1948.

991 Messer, H., Zinevich, A., and Alpert, P.: Environmental monitoring by wireless communication  
992 networks, *Science*, 312, 713–713, <https://doi.org/10.1126/science.1120034>, 2006.

993 Michelson, D., Henja, A., Ernes, S., Haase, G., Koistinen, J., Ośródkka, K., Peltonen, T., Szewczykowski,  
994 M., and Szturc, J.: BALTRAD Advanced Weather Radar Networking, *J. Open Res. Softw.*, 6, 12,  
995 <https://doi.org/10.5334/jors.193>, 2018.

996 Michelson, D. B. and Koistinen, J.: Gauge-Radar network adjustment for the Baltic Sea experiment,  
997 *Phys. Chem. Earth Part B Hydrol. Oceans Atmosphere*, 25, 915–920, [https://doi.org/10.1016/S1464-1909\(00\)00125-8](https://doi.org/10.1016/S1464-1909(00)00125-8), 2000.

999 Michelson, D. B., Lewandowski, R., Szewczykowski, M., Beekhuis, H., and Haase, G.: EUMETNET  
1000 OPERA weather radar information model for implementation with the HDF5 file format, version 2.2,  
1001 2014.

1002 Mobini, S., Nilsson, E., Persson, A., Becker, P., and Larsson, R.: Analysis of pluvial flood damage costs  
1003 in residential buildings – A case study in Malmö, *Int. J. Disaster Risk Reduct.*, 62, 102407,  
1004 <https://doi.org/10.1016/j.ijdrr.2021.102407>, 2021.

1005 Nielsen, J. M., van de Beek, C. Z. R., Thorndahl, S., Olsson, J., Andersen, C. B., Andersson, J. C. M.,  
1006 Rasmussen, M. R., and Nielsen, J. E.: Merging weather radar data and opportunistic rainfall sensor  
1007 data to enhance rainfall estimates, *Atmospheric Res.*, 300, 107228,  
1008 <https://doi.org/10.1016/j.atmosres.2024.107228>, 2024.

1009 Olsson, J., Södling, J., Berg, P., Wern, L., and Eronn, A.: Short-duration rainfall extremes in Sweden: a  
1010 regional analysis, *Hydrol. Res.*, 50, 945–960, <https://doi.org/10.2166/nh.2019.073>, 2019.

1011 Overeem, A., Leijnse, H., and Uijlenhoet, R.: Two and a half years of country-wide rainfall maps using  
1012 radio links from commercial cellular telecommunication networks, *Water Resour. Res.*, 52, 8039–  
1013 8065, <https://doi.org/10.1002/2016WR019412>, 2016.

1014 Overeem, A., Leijnse, H., van der Schrier, G., van den Besselaar, E., Garcia-Marti, I., and de Vos, L. W.:  
1015 Merging with crowdsourced rain gauge data improves pan-European radar precipitation estimates,  
1016 *Hydrol. Earth Syst. Sci.*, 28, 649–668, <https://doi.org/10.5194/hess-28-649-2024>, 2024.

1017 Øydvin, E., Graf, M., Chwala, C., Wolff, M. A., Kitterød, N.-O., and Nilsen, V.: Technical note: A simple  
1018 feedforward artificial neural network for high-temporal-resolution rain event detection using signal  
1019 attenuation from commercial microwave links, *Hydrol. Earth Syst. Sci.*, 28, 5163–5171,  
1020 <https://doi.org/10.5194/hess-28-5163-2024>, 2024.

1021 Petersson, L., ten Veldhuis, M.-C., Verhoeven, G., Kapelan, Z., Maholi, I., and Winsemius, H. C.:  
1022 Community mapping supports comprehensive urban flood modeling for flood risk management in a  
1023 data-scarce environment, *Front. Earth Sci.*, 8, <https://doi.org/10.3389/feart.2020.00304>, 2020.

1024 Polz, J., Chwala, C., Graf, M., and Kunstmann, H.: Rain event detection in commercial microwave link  
1025 attenuation data using convolutional neural networks, *Atmospheric Meas. Tech.*, 13, 3835–3853,  
1026 <https://doi.org/10.5194/amt-13-3835-2020>, 2020.

1027 Polz, J., Graf, M., and Chwala, C.: Missing rainfall extremes in commercial microwave link data due to  
1028 complete loss of signal, *Earth Space Sci.*, 10, e2022EA002456,  
1029 <https://doi.org/10.1029/2022EA002456>, 2023.

1030 Pulkkinen, S., Nerini, D., Pérez Hortal, A. A., Velasco-Forero, C., Seed, A., Germann, U., and Foresti, L.:  
1031 Pysteps: an open-source Python library for probabilistic precipitation nowcasting (v1.0), *Geosci.  
1032 Model Dev.*, 12, 4185–4219, <https://doi.org/10.5194/gmd-12-4185-2019>, 2019.

1033 Rayitsfeld, A., Samuels, R., Zinevich, A., Hadar, U., and Alpert, P.: Comparison of two methodologies  
1034 for long term rainfall monitoring using a commercial microwave communication system, *Atmospheric  
1035 Res.*, 104–105, 119–127, <https://doi.org/10.1016/j.atmosres.2011.08.011>, 2012.

1036 Schleiss, M. and Berne, A.: Identification of dry and rainy periods using telecommunication  
1037 microwave links, *IEEE Geosci. Remote Sens. Lett.*, 7, 611–615,  
1038 <https://doi.org/10.1109/LGRS.2010.2043052>, 2010.

1039 Seo, D.-J., Breidenbach, J., Fulton, R., Miller, D., and O’Bannon, T.: Real-time adjustment of range-  
1040 dependent biases in WSR-88D rainfall estimates due to nonuniform vertical profile of reflectivity, *J.  
1041 Hydrometeorol.*, 1, 222–240, [https://doi.org/10.1175/1525-  
1042 7541\(2000\)001%253C0222:RTAORD%253E2.0.CO;2](https://doi.org/10.1175/1525-7541(2000)001%253C0222:RTAORD%253E2.0.CO;2), 2000.

1043 SMHI: [https://www.smhi.se/nyheter/nyheter/2020-11-20-tradtoppar-orsakar-blockeringar-for-  
1044 vaderradar-angelholm](https://www.smhi.se/nyheter/nyheter/2020-11-20-tradtoppar-orsakar-blockeringar-for-vaderradar-angelholm), last access: 18 March 2025a.

1045 MEMO: [https://www.smhi.se/en/research/about-us/open-access-to-data-for-research-and-  
1046 development/memo](https://www.smhi.se/en/research/about-us/open-access-to-data-for-research-and-development/memo), last access: 15 April 2025.

1047 SMHI: <https://www.smhi.se/data/nederbord-och-fuktighet/nederbord>, last access: 14 April 2025b.

1048 SMHI: [https://www.smhi.se/data/nederbord-och-fuktighet/nederbord/radarbilder-aktuella-och-  
1049 historiska](https://www.smhi.se/data/nederbord-och-fuktighet/nederbord/radarbilder-aktuella-och-historiska), last access: 14 April 2025c.

1050 SMHI:  
1051 [https://www.smhi.se/pd/klimat/time\\_period\\_maps/normal/Nbd\\_Periodnormal/Nbd\\_Periodnormal\\_  
1052 1991\\_2020\\_ar.png](https://www.smhi.se/pd/klimat/time_period_maps/normal/Nbd_Periodnormal/Nbd_Periodnormal_1991_2020_ar.png), last access: 10 November 2025d.

1053 Sovacool, B. K. and Furszyfer Del Rio, D. D.: Smart home technologies in Europe: A critical review of  
1054 concepts, benefits, risks and policies, *Renew. Sustain. Energy Rev.*, 120, 109663,  
1055 <https://doi.org/10.1016/j.rser.2019.109663>, 2020.

1056 Thorndahl, S., Einfalt, T., Willems, P., Nielsen, J. E., ten Veldhuis, M.-C., Arnbjerg-Nielsen, K.,  
1057 Rasmussen, M. R., and Molnar, P.: Weather radar rainfall data in urban hydrology, *Hydrol. Earth Syst.  
1058 Sci.*, 21, 1359–1380, <https://doi.org/10.5194/hess-21-1359-2017>, 2017.

1059 UN-Habitat: World Cities Report 2024, United Nations Human Settlements Programme (UN-Habitat),  
1060 2024.

1061 Foreningen VeVa – Vejrradar i vandsektoren: <https://veva.dk/>, last access: 19 May 2025.

1062 de Vos, L. W., Raupach, T. H., Leijnse, H., Overeem, A., Berne, A., and Uijlenhoet, R.: High-resolution  
1063 simulation study exploring the potential of radars, crowdsourced personal weather stations, and  
1064 commercial microwave links to monitor small-scale urban rainfall, *Water Resour. Res.*, 54, 10,293-  
1065 10,312, <https://doi.org/10.1029/2018WR023393>, 2018.

Formatted: English (United States)

1066 de Vos, L. W., Leijnse, H., Overeem, A., and Uijlenhoet, R.: Quality control for crowdsourced personal  
1067 weather stations to enable operational rainfall monitoring, *Geophys. Res. Lett.*, 46, 8820–8829,  
1068 <https://doi.org/10.1029/2019GL083731>, 2019.

1069 Wang, Z., Schleiss, M., Jaffrain, J., Berne, A., and Rieckermann, J.: Using Markov switching models to  
1070 infer dry and rainy periods from telecommunication microwave link signals, *Atmospheric Meas.*  
1071 *Tech.*, 5, 1847–1859, <https://doi.org/10.5194/amt-5-1847-2012>, 2012.

1072 Winsemius, H. C., Jongman, B., Veldkamp, T. I. E., Hallegatte, S., Bangalore, M., and Ward, P. J.:  
1073 Disaster risk, climate change, and poverty: assessing the global exposure of poor people to floods  
1074 and droughts, *Environ. Dev. Econ.*, 23, 328–348, <https://doi.org/10.1017/S1355770X17000444>, 2018.

Formatted: English (United States)

1075 Wolf, T. and Larsson, R.: Privata regnmätare för professionell användning– Test av Netatmo  
1076 regnsensor i Trelleborg och Svedala, *Tidsskr. Vatten*, 3, 2024.

1077